

1 Impacts of Secondary Ice Production on Arctic Mixed-Phase
2 Clouds based on ARM Observations and CAM6 Single-
3 Column Model Simulations

删除了: CESM2

4
5 Xi Zhao¹, Xiaohong Liu¹, Vaughan T. J. Phillips², and Sachin Patade²

6 ¹Department of Atmospheric Sciences, Texas A&M University, College Station, Texas, 77840, USA

7 ²Department of Physical Geography and Ecosystem Science, Lund University, Lund, Sweden

8
9 *Correspondence to:* Xiaohong Liu (xiaohong.liu@tamu.edu)

10 **Abstract.** For decades, measured ice crystal number concentrations have been found to be orders
11 of magnitude higher than measured ice nucleating particle number concentrations in moderately
12 cold clouds. This observed discrepancy reveals the existence of secondary ice production (SIP) in
13 addition to the primary ice nucleation. However, the importance of SIP relative to primary ice
14 nucleation remains highly unclear. Furthermore, most weather and climate models do not represent
15 well the SIP processes, leading to large biases in simulated cloud properties. This study
16 demonstrates a first attempt to represent different SIP mechanisms (frozen raindrop shattering, ice-
17 ice collisional break-up, and rime splintering) in a global climate model (GCM). The model is run
18 in the single column mode to facilitate comparisons with the Department of Energy (DOE)'s

删除了: ↵

21 Atmospheric Radiation Measurement (ARM) Mixed-Phase Arctic Cloud Experiment (M-PACE)

22 observations.

23 We show the SIP importance in the four types of clouds during M-PACE (i.e., multilayer clouds,

24 single-layer stratus, transition and frontal clouds), with the maximum enhancement in ice crystal

25 number concentrations by up to 4 orders of magnitude in moderately supercooled clouds. We reveal

26 that SIP is the dominant source of ice crystals near the cloud base for the long-lived Arctic single-

27 layer mixed-phase clouds. The model with SIP improves the occurrence and phase partitioning of

28 the mixed-phase clouds, reverses the vertical distribution pattern of ice number concentrations, and

29 provides a better agreement with observations. The findings of this study highlight the importance

30 of considering the SIP in GCMs.

31

32

删除了: and

删除了: the

删除了: -

删除了: cold

37 **1 Introduction**

38 Clouds play a critical role in the surface energy budget of the Arctic, thereby
39 affecting the Arctic sea ice and regional climate (Kay et al., 2009; Bennartz et al., 2013).

40 Clouds occur frequently in the Arctic (Beaufort Sea) with an observed annual mean
41 occurrence of 85%, a maximum of 97% in September, and a minimum of 63% in February

删除了: frequently

删除了: cloud

42 (Intrieri et al., 2002). Along with the occurrence frequency, the phase partitioning between
43 liquid and ice in mixed-phase clouds, i.e., the clouds where liquid and ice coexist at
44 subfreezing temperatures, is also important, since even a small amount of liquid content in
45 clouds can substantially change the radiative properties of the cloud (Shupe et al., 2004;

46 Cesana and Chepfer, 2013). Shupe et al. (2006) showed that over the Beaufort Sea, 59%
47 of observed clouds were mixed-phase, while another study indicated 90% over the western

删除了: , furthermore, cloud properties further play a key role in the Arctic climate change through cloud feedbacks (Vavrus, 2004; Zhang et al., 2018; Tan and Storelvmo, 2019).

48 Arctic Basin (Pinto, 1998). Cloud properties further play a key role in the Arctic climate
49 change through cloud feedbacks (Vavrus, 2004; Zhang et al., 2018; Tan and Storelvmo,
50 2019).

51 Mixed-phase clouds are microphysically unstable. Even a small amount of cloud
52 ice can glaciare the mixed-phase clouds in a few hours via the Wegener–Bergeron–
53 Findeisen (WBF) mechanism (Morrison et al., 2012). Mixed-phase clouds in the Arctic are
54 long-lived and characterized by a structure with liquid water at the cloud top and ice water
55 underneath. Interaction and feedback among multiple processes, including longwave

删除了: between

62 radiative cooling, turbulence, entrainment, and condensation of liquid water, provide
63 sufficient moistening and cooling at the cloud top. This sustains enough formation of liquid
64 mass against the depletion by the WBF process. In order to support the self-maintenance
65 of liquid water, low concentrations of small ice particles must be present near the cloud
66 base (Shupe et al., 2006; Korolev and Field, 2008). In this way, they are efficient in
67 sedimentation (Jiang et al., 2000) but less active in the WBF and vapor deposition
68 processes. Previous studies indicated that 90% of Arctic mixed-phase cloud temperatures
69 were between -25°C and -5°C from an annual mean perspective (Shupe et al., 2006),
70 indicating that ice exists in moderately supercooled clouds. However, the mechanisms
71 contributing to ice formation in these clouds are still unclear (Shupe et al., 2006; Morrison
72 et al., 2012). One objective of this study is to better understand the ice formation processes
73 in the Arctic mixed-phase clouds.

删除了: t

删除了: was

删除了: Arctic

74 Previous studies have shown the important role of SIP in the Arctic clouds from
75 observations (Schwarzenboeck et al., 2009) and small-scale model simulations
76 (Sotiropoulou et al., 2020a; Fu et al., 2019). Using a large-eddy simulation (LES) model
77 and a Lagrangian parcel model, Sotiropoulou et al. (2020a) found that a combination of
78 ice-ice collisional fragmentation and rime splintering provides a better agreement of the
79 simulated ice crystal number concentrations (ICNCs) with observations in the summer
80 Arctic stratocumulus. They found a low sensitivity of SIP to prescribed number
81 concentrations of cloud condensation nuclei (CCN) and ice nucleating particles (INPs). Fu

删除了: In addition, their study highlighted the importance of considering ice-ice collisional fragmentation in large-scale models.

88 et al. (2019) simulated an autumnal Arctic single-layer boundary-layer mixed-phase cloud
89 using the Weather Research and Forecasting (WRF) model and showed that the model
90 without considering SIP needs an increase of INP concentrations by two orders of
91 magnitude to match the observed ICNCs. In comparison, the model that only considers the
92 SIP through droplet shattering needs an INP increase of 50 times to match the observed
93 ICNCs.

94 The roles of SIP have also been investigated in other geographical regions and for
95 other cloud types. Sotiropoulou et al. (2020b) simulated a summer boundary layer coastal
96 cloud in West Antarctica using the WRF model and found that the model with collisional
97 break-up between ice-phase particles can reproduce the observed ICNCs, which could not
98 be explained by the rime splintering or primary ice nucleation. Sullivan et al. (2017) used
99 a parcel model with rime splintering and graupel-graupel collisional break-up and found
100 that these two SIP processes can enhance the ICNCs by four orders of magnitude. Sullivan
101 et al. (2018a) showed that among the different SIP mechanisms, only ice-ice collisional
102 fragmentation contributes to a meaningful ice enhancement (larger than 0.002 L^{-1}) in a
103 parcel model simulation. Other studies have shown the impact of SIP on ICNCs in a cold
104 frontal rain band over the UK (Sullivan et al., 2018b), on surface precipitation of a tropical
105 thunderstorm (Connolly et al., 2006), and on the summertime cyclones (Dearden et al.,
106 2016).

删除了: They also found that a modest updraft and a warm cloud base significantly affect the onset of rime splintering and droplet shattering.

110 Previous modeling studies have used small-scale (e.g., parcel models and LES
111 models) and regional-scale models, to investigate the impacts of SIP on cloud properties.
112 There is still a lack of large-scale perspective based on global climate models (GCMs).
113 Moreover, the mechanisms contributing to ice production in the Arctic mixed-phase clouds
114 at moderately cold temperatures are still unknown. In this study, for the first time, we
115 implemented the representation of two new SIP mechanisms (i.e., raindrop shattering, ice-
116 ice collisional break-up) in a GCM. We tested the model performance by running the model
117 in the single column mode (SCM) and compared the SCM simulations of Arctic clouds
118 with observations. The objectives of this study are to examine the impact of SIP on different
119 types of the Arctic clouds and, ultimately to improve the model capability of representing
120 ice processes.

121 This paper is organized as follows. In section 2, we describe the GCM, associated
122 parameterizations, and the three SIP mechanisms represented in the model. In section 3,
123 we present the model experiments and observation data used for model evaluation. The
124 model results are presented in section 4. The main conclusions of this study and future
125 work are summarized in section 5.

删除了: multi-scale models, including

删除了: models

删除了: such as

删除了: ,

删除了: as well as

删除了: However, t

删除了: a

删除了:

删除了: a

删除了: the

删除了: have

删除了: multiple

删除了: , and rime splintering

删除了: global climate model (

删除了:)

删除了: and 6

142 2 Model and Parameterizations

143 2.1 Model description

144 The Community Atmosphere Model version 6 (CAM6) used in ~~this~~ study is the
145 atmosphere component of the Community Earth System Model version 2 (CESM2). It
146 includes multiple physical parameterizations that are related to ice formation and evolution.

147 Cloud microphysics is described by a double-moment ~~scheme~~ (Gettelman and Morrison,
148 2015, ~~hereafter as MG~~). The scheme considers homogeneous freezing of cloud droplets
149 (with temperatures below $-40\text{ }^{\circ}\text{C}$), heterogeneous freezing of cloud droplets, the ~~WBF~~
150 process, accretion of cloud droplets by snow, and the ~~rime~~ splintering. ~~SIP~~ from rime

151 splintering is parameterized based on Cotton et al. (1986). The condensation process is also
152 known as cloud macrophysics, which is governed by the Cloud Layers Unified by Binormals
153 (CLUBB) scheme, assuming that all the condensate is in the liquid phase (Golaz et al., 2002;
154 Larson et al., 2002). Furthermore, CLUBB also treats boundary layer turbulence and shallow
155 convection. In the mixed-phase clouds, heterogeneous ice nucleation is represented by the
156 classical nucleation theory (CNT), which relates ice nucleation rate to mineral dust and black
157 carbon aerosols (Wang et al., 2014). In cirrus clouds, where temperatures are below $-37\text{ }^{\circ}\text{C}$,
158 heterogeneous immersion freezing on dust can compete with homogeneous freezing of
159 sulfate (Liu and Penner, 2005). The aerosol species involved in ice nucleation processes are

删除了: e

删除了: current

删除了: microphysical

删除了: based on

删除了:

删除了: Wegener-Bergeron-Findeisen

删除了: ing

删除了: Secondary ice production

168 represented by the four-mode version of the Modal Aerosol Module (MAM4) (Liu et al.,
169 2012; Liu et al., 2016).

170 In this study, we conducted the simulations using the SCM version of CAM6 (i.e.,
171 SCAM). SCAM is a one-column, time-dependent model configuration of CAM6 that
172 provides an efficient way to understand the behavior of model physical parameterizations
173 without the influence of nonlinear feedbacks from the large-scale circulation. In this way, the
174 biases of the modeled clouds can be exclusively identified from model evaluation against
175 observations.

删除了: have

删除了: CAM6

删除了: in

176 2.2 Implementation of secondary ice production in CESM2

177 In addition to the existing SIP mechanism (i.e., rime splintering), in CAM6, we
178 implemented two new mechanisms of SIP, including ice-ice fragmentation and droplet
179 shattering (Phillips et al., 2017a, 2018) that are parameterized based on theoretical and
180 measurement research.

删除了: s

181 a. An emulated bin framework

182 Ideally, a bin microphysics scheme is the most suitable model setup for the
183 representation of SIP mechanisms in a model. However, running a GCM model with a bin
184 microphysics scheme is computationally too expensive under current computational
185 resources. To solve this problem, we developed an emulated bin framework for the existing

删除了: cloud

191 bulk MG microphysics scheme to facilitate the collisions of ice hydrometeors and
192 raindrops. First, we selected the bin bounds for each hydrometeor, including cloud ice,
193 snow, and rain. A logarithmically equidistant size grid is adopted, that is,

删除了: microphysical
删除了: coagulation

194
$$D_{k+1} = CD_k, \quad (1)$$

195 where $C = \sqrt[4]{2}$. The bin diameter ranges from 0.1 to 6 mm for raindrops and 0.1 to 50 mm
196 for snow and cloud ice particles. Based on the assumption of the particle size distribution,
197 the number concentration and mass mixing ratio of all hydrometeor types were calculated
198 in each temporary bin at each time step and grid point. The estimated particle size
199 distribution from the emulated bin framework served as inputs for the SIP schemes. The
200 SIP schemes were applied to each permutation of the bin during collisions of ice, snow,
201 and rain to calculate the secondary ice fragments. Finally, we summed up the fragment
202 from SIP over all pairs of bins.

删除了:
删除了: ←
带格式的: 缩进: 首行缩进: 0 字符
删除了: was
删除了: s
删除了: serves
删除了: coagulation

203 The bin approach is only adopted in the SIP processes, while other processes,
204 including the existing collisions in the standard MG scheme, still use the bulk
205 microphysical approach. Thus, the modified MG scheme becomes a hybrid scheme that
206 combines the bulk and bin parameterizations. The advantage of this hybrid scheme is that
207 the scheme can provide an accurate representation of the SIP processes while still maintains
208 a relatively high computational efficiency, which is very important for GCMs. The hybrid
209 schemes have been widely used. For example, previous studies used the bin approach for
210 the warm rain processes, while adopted the bulk approach for the ice-related processes

删除了: global climate models

220 ([Onishi and Takahashi, 2012](#); [Grabowski et al., 2010](#); [Kuba and Murakami, 2010](#)). Other
221 [previous studies used the bin approach for the sedimentation \(Morrison, 2012\)](#) or look-up
222 [tables for the collision processes in the bulk schemes \(Feingold et al., 1998\)](#).

223

224 **b. Ice-ice fragmentation**

225 Phillips et al. (2017a, b) developed a scheme for SIP during an ice-ice collision
226 based on the principle of energy conservation. This scheme relates the fragment numbers
227 to particle initial kinetic energy and ice particle habits (i.e., ice morphology), which can be
228 explained in terms of environmental temperature, particle size, and riming intensity of ice
229 particles (Fig. 1). The production of new ice particles per collision is calculated as:

230

$$231 \quad \mathcal{N} = \alpha A \left[1 - e^{-\left(\frac{Ck_0}{\alpha A}\right)^\gamma} \right] \quad (2)$$

232

233 in which α is the surface area of ice particle, i.e., the equivalent spherical area in a unit of
234 m^2 , $\alpha = \pi D^2$; A is the number density of breakable asperities of ice particles, which is
235 related to riming intensity and ice particle size; C is the asperity-fragility coefficient,
236 prescribed to be 10815 for dendrites and 24780 for spatial planar; γ is a parameter related
237 to riming intensity (rim), $\gamma = 0.5 - (0.25 \times rim)$, and rim is assumed to be 0.1; k_0 is
238 the initial kinetic energy, which is given as:

239
$$k_0 = \frac{1}{2} \frac{m_1 m_2}{m_1 + m_2} (v_1 - v_2)^2 \quad (3)$$

240 in which m_1 and m_2 are the particle masses of two colliding particles, and v_1 and v_2
241 are the terminal velocities of the two colliding particles.

242 In this method, three types of collision are identified based on the type of collision
243 particles: (1) cloud ice/snow collide with hail/graupel; (2) cloud ice/snow collide with
244 cloud ice/snow; (3) hail/graupel collide with hail/graupel (not included currently, since
245 CESM2-CAM6 does not treat graupel currently). For each collision type, different values
246 of parameters α , A , C , and γ in Eq. (2) are yielded based on the measured relationship
247 between fragment number and collisional kinetic energy (Phillips et al., 2017a).

248 Under the emulated bin framework, the new fragment production rate for each
249 permutation of a bin is written as:

250
$$N_{iic} = \mathcal{N} E_c \delta N_1 \delta N_2 \pi (r_1 + r_2)^2 |v_1 - v_2| \quad (4)$$

251 in which E_c is the accretion efficiency, [assumed to be 0.5 to be consistent with the MG](#)
252 [microphysics scheme](#), and δN_1 and δN_2 are the particle number concentrations in the
253 two bins with particle sizes of r_1 and r_2 , respectively.

254 The ice production rate for cloud ice mixing ratio is:

255
$$P_{iic} = N_{iic} \delta m_{ice} \quad (5)$$

256 in which δm_{ice} is mass for single ice particle, prescribed as 2.09×10^{-15} kg.

删除了: .

删除了: 1

删除了: al

260 c. Droplet shattering during rain freezing

261 Phillips et al. (2018) proposed numerical formulations for ice multiplication during
262 the raindrop freezing. They suggested two modes of droplet break-up during the rain
263 freezing based on the relative weight of raindrop and ice particle (Fig. 2).

264 In mode 1, the freezing of rain is triggered by a collision with less massive ice
265 crystals or with INPs. By fitting to the laboratory data, Phillips et al. (2018) derived an
266 empirical formulation for the number of ice fragments per frozen raindrop as a function of
267 drop diameter and temperature. A Lorentzian distribution as a function of temperature was
268 adopted to represent the number of ice fragments per frozen raindrop. There are two types
269 of raindrop fragmentation: shattering to form “large” fragments and “tiny” splinters. The
270 total (large, plus tiny) and big ice fragments per frozen raindrop emitted in the mode 1 of
271 droplet shattering are given in Eqs. (6) and (7), respectively:

$$272 \quad \mathcal{N}_T = F(D)\Omega(T) \left[\frac{\zeta\eta^2}{(T-T_0)^2 + \eta^2} + \beta T \right] \quad (6)$$

$$273 \quad \mathcal{N}_B = \min \left\{ F(D)\Omega(T) \left[\frac{\zeta_B\eta_B^2}{(T-T_{B0})^2 + \eta_B^2} \right], \mathcal{N}_T \right\} \quad (7)$$

274 where the parameters $\zeta, \eta, \beta, \zeta_B, \eta_B, T_0, T_{B0}$ are derived by fitting the formulations to a
275 collection of laboratory data. Further details about empirical formulae can be found in
276 Phillips et al. (2018). $F(D)$ and $\Omega(T)$ are the interpolating functions for the onset of
277 fragmentation and T is the temperature in K. The mass of a big fragment is $m_B = \chi_B m_{rain}$.

删除了: a

删除了: a formulation

删除了: set

删除了: broken halves or a third of similar sizes known as

删除了: '

删除了: '

删除了: '

删除了: '

删除了: with less than 10% of the original drop mass

删除了: +

删除了: large

删除了: on

删除了: tion

删除了: large

292 in which $\chi_B = 0.4$, and the mass of a small fragment is $m_s = \frac{\pi\rho_i}{6}D^3$, in which $\rho_i =$
293 500 kg m^{-3} .

删除了: 92

294 The observational data used for the formulations of raindrop freezing by mode 1
295 was limited to drop diameter of 1.6 mm and a temperature range between -4°C to -25°C .
296 Phillips et al. (2018) linearly extrapolated their algorithm for larger particles and other
297 temperatures in the mixed-phase cloud regime. As shown in Fig. 2a, b, mode 1 of the
298 droplet shattering is most effective near -15°C .

删除了: for mode 1

删除了: the

299 In mode 2, a theoretical approach is adopted which is based on the assumption that
300 the number of fragments generated when a drop collides with a more massive ice particle
301 is controlled by the initial kinetic energy and surface energy (Fig. 2c). The number of
302 fragments generated per frozen drop in mode 2 is given as:

删除了: i

$$303 \quad \mathcal{N}_{fr2} = 3\Phi(T) \times [1 - f(T)] \times \max(DE - DE_c), \quad (8)$$

304 where DE is the dimensionless energy and is expressed as:

$$305 \quad DE = \frac{k_0}{S_e}, \quad (9)$$

306 where k_0 is the initial kinetic energy which is given in Eq. (3), S_e is the surface energy,
307 expressed as $S_e = \gamma_{liq}\pi D^2$ (for $D > 150 \mu\text{m}$), γ_{liq} is the surface tension of liquid water
308 which is 0.073 J m^{-2} . DE_c in Eq. (8) is set to be 0.2. $f(T)$ is the frozen fraction (Phillips
309 et al., 2018), and is given as:

314
$$f(T) = \frac{-C_w T}{L_f}. \quad (10)$$

315 where C_w is the specific heat capacity of liquid water ($4200 \text{ J kg}^{-1} \text{ K}^{-1}$) and L_f is the specific
 316 latent heat of freezing ($3.3 \times 10^5 \text{ J kg}^{-1}$), $\Phi(T) = 0.5$ at -1°C and $\Phi(T) = \min [4f(T), 1]$.

317 **d. Rime splintering**

318 The **MG** microphysics already includes the SIP associated with rime splintering,
 319 which is also known as Hallet-Mossop (HM) process. In this process, secondary ice
 320 particles are generated during the accretion of cloud droplets by snow, and a part of rimed
 321 mass is converted to cloud ice. The ice number production rate is based on the
 322 parameterization of Cotton et al. (1986), which is given as:

323
$$N_{HM} = C_{sip_HM} \times p_{sacws} \quad (11)$$

324 where p_{sacws} is the riming rate of cloud droplets by snow and is expressed as:

325
$$p_{sacws} = \frac{\pi \times a_{vs} \times \rho \times N_{0s} \times E_{ci} \times \Gamma (b_{vs} + 3)}{4 \times \lambda^{b_{vs} + 3}} \quad (12)$$

326 in which E_{ci} is the collection efficiency for the riming of cloud droplets by snow, a_{vs}
 327 and b_{vs} are the fall speed parameters for snow particles, $b_{vs} = 0.41$, and $a_{vs} =$
 328 $11.72 \times \frac{\rho_{850}}{\rho}$, ρ and ρ_{850} are air density and typical air density at 850 hPa, respectively,
 329 and N_{0s} and λ are the parameters for the snow particle size distribution.

330 The conversion coefficient C_{sip_HM} in Equation (11) depends on temperature T_c
 331 in $^\circ\text{C}$:

332
$$C_{sip_HM} = \frac{3.5 \times 10^8 \times (-3 - T)}{2}, \text{ when } -5 < T_c < -3, \text{ and} \quad (13)$$

设置了格式: 字体: 倾斜

删除了: .

设置了格式: 字体: 倾斜

删除了: CESM2-CAM6

删除了: ing

删除了: and

带格式的: 两端对齐

删除了: the

删除了: the

删除了: ↵

带格式的: 左, 缩进: 首行缩进: 0 字符

删除了: , and

删除了: t

删除了: 12

$$C_{sip_{HM}} = \frac{3.5 \times 10^8 \times (T - (-8))}{3}, \text{ when } -8 < T_c < -5 \quad (14)$$

The production rate for cloud ice mixing ratio is given as:

$$P_{HM} = N_{HM} \delta m_{ice} \quad (15)$$

in which δm_{ice} is mass for single ice particle in the HM process, prescribed as 2.09×10^{-15}

kg. The rim splintering rate as a function of p_{sacws} and temperature is shown in Fig. 3.

3 Case Description, Observations, and Model Experiments

3.1 M-PACE case

In this study, we focus on the Arctic mixed-phase clouds observed during the Department of Energy (DOE)'s Atmospheric Radiation Measurement (ARM) Mixed-Phase Arctic Cloud Experiment (M-PACE). The M-PACE campaign was conducted over the North Slope of Alaska (NSA) during the autumn from 27 September to 22 October 2004.

Various types of clouds were observed during M-PACE, including multilayer clouds, boundary layer mixed-phase stratus, cirrus, and altostratus clouds associated with the frontal system (Verlinde et al., 2007; Liu et al., 2007; Xie et al., 2008; Liu et al., 2011). Single-layer mixed-phase clouds were formed under moderately supercooled conditions with the cloud temperature at around -10 °C (Verlinde et al., 2007; McFarquhar et al., 2007), providing a favorable condition for studying the influence of SIP on cloud evolution (Field et al., 2016).

删除了: 13

删除了: ice

带格式的: 缩进: 首行缩进: 0 字符

删除了: ing

删除了: period

删除了: campaign

删除了: stratus

删除了: thin

删除了: clouds

369 The synoptic-scale systems regulated the properties of clouds observed during the M-
370 PACE campaign. Hence, Verlinde et al. (2007) divided the M-PACE period into three
371 synoptic regimes and two transition periods based on the synoptic weather conditions. The
372 first synoptic regime began on 24 September and lasted until 1 October, 2004, when a well-
373 developed trough dominated aloft with several low-pressure systems that influenced the
374 surface. Followed by the first transition period between 2 and 3 October, the second synoptic
375 regime occurred between 4 and 14 October (Fig. 4), which was controlled by a pronounced
376 high-pressure system. The second transition period was from 15-17 October. By 18 October,
377 a fast-developing strong frontal system controlled the cloud formation over the NSA in the
378 third synoptic regime (Fig. 4). During M-PACE, the surface flux of water vapor, sensible
379 heat, and latent heat played different roles in the cloud formation. For example, clouds
380 formed in response to a strong surface forcing during the second regime, while clouds formed
381 under a relatively weak surface forcing during the third regime. In this study, we evaluate the
382 modeled cloud properties with M-PACE observations in the second and third synoptic
383 regimes focusing on the boundary layer mixed-phase stratus during 9-12 October in the
384 second regime.

385 3.2 Observation data

386 The observed cloud occurrence data at Barrow (located at 71.3° N, 156.6° W) are
387 from the ARM Climate Modeling Best Estimate product (Xie et al., 2010). The liquid water

删除了: a

删除了: :

390 path (LWP) and ice water path (IWP) data are obtained from Zhao et al. (2012).
 391 Specifically, the Shupe and Turner's data are based on the retrievals of cloud properties
 392 measured by the ARM Millimeter-Wavelength Cloud Radar (Shupe et al., 2005) and the
 393 Microwave Radiometer (MWR) (Turner et al., 2007), with the uncertainties for liquid water
 394 content (LWC) within 50% and for ice water content (IWC) within a factor of 2. For
 395 Wang's data, IWP is retrieved from the combined ARM Millimeter-Wavelength Cloud
 396 Radar and Micropulse lidar measurements (Wang and Sassen, 2002) with an uncertainty
 397 of 35% (Khanal and Wang, 2015). LWP is retrieved from the ARM MWR measurements
 398 with an uncertainty of 50% (Wang, 2007). For Deng's data, IWC is retrieved based on the
 399 Millimeter-Wavelength Cloud Radar measurements, with a retrieval error within 85%
 400 (Deng and Mace, 2006). For Dong's data, LWC is retrieved from the MWR measurements
 401 with an uncertainty within 113% (Dong and Mace, 2003). Note that measured IWC and
 402 IWP cannot distinguish cloud ice from the snow. The simulated IWP and IWC therefore
 403 include the snow component which is consistent with observations used in this study.

404 The ICNC was measured during the M-PACE single-layer mixed-phase stratus
 405 period. The data includes 53 profiles measured in four flights over Barrow and Oliktok Point
 406 (located at 70.5° N, 149.9° W) by the University of North Dakota Citation aircraft. By
 407 combining measurements from different probes, McFarquhar et al. (2007) provided cloud
 408 particle size distributions over a continuous size range. The forward scattering spectrometer
 409 probe (FSSP) measured particle number concentrations with particle diameters between 3 to

- 删除了: LWP
- 删除了: IWP
- 删除了: a 35-GH millimeter cloud radar
- 删除了: IWC
- 删除了: the
- 删除了:
- 删除了: m
- 删除了: Microwave Radiometer (
- 删除了:)
- 删除了: m
- 删除了: w
- 删除了: Doppler r
- 删除了: ,
- 删除了: the
- 删除了: algorithm
- 删除了: for IWC
- 删除了: derived
- 删除了: microwave radiometer
- 批注 [LX2]: Please check the accuracy
- 删除了: the
- 删除了: The liquid water path (LWP) was measured using the ARM Climate Facility operational Microwave Radiometer with different retrieved algorithms (Wang 2007; Turner et al., 2007). The ice water path (IWP) was using the ... [1]
- 删除了: ice water content (
- 删除了:)
- 删除了: During M-PACE campaign, t
- 删除了: during
- 删除了: :
- 删除了: using the instrumented aircraft

445 53 μm , while the one-dimensional cloud probe (1DC) counted cloud particles ranging from
446 20 to 620 μm . The two-dimensional cloud probe (2DC) covered particle sizes from 30 to 960
447 μm , while the high-volume precipitation sampler (HVPS) sampled particles from 0.4 to 40
448 mm. The data were collected every 10 seconds but were averaged to 30 s^{-1} to ensure adequate
449 statistical sampling. The cloud phase was identified by detecting the presence of supercooled
450 droplets by the Rosemount Icing Detector (RICE). In mixed-phase clouds, any particles
451 larger than 125 μm are identified as ice particles, and cloud particles smaller than 53 μm are
452 counted as liquid-phase particles. Particles with a diameter ranging from 53 to 125 μm are
453 counted as a liquid when there is drizzle, and as ice, if there is no drizzle. A more detailed
454 description of the particle phase identification algorithm can be found in McFarquhar et al.
455 (2007). When comparing the simulated ICNC with the observations, we only consider ice
456 particles larger than 53 μm , as the observations were limited to ice particles larger than 53
457 μm .

删除了: should

删除了: were considered

删除了:

458 However, the M-PACE data were collected before the advent of shatter mitigating
459 tips and before algorithms for removing the shattered particles had been developed. Thus,
460 there are no corrections for the shattering effect in these data. Previous studies indicated an
461 averaged reduction of ice number concentrations by 1-4.5 times and up to a factor of 10
462 (for some data samples) in other field campaigns, such as the Instrumentation Development
463 and Education in Airborne Science 2011 (IDEAS-2011), the Holographic Detector for
464 Clouds (HOLODEC), and the Indirect and Semidirect Aerosol Campaign (ISDAC), which

468 also used the 2DC cloud probe, but adopted anti-shattering tips and algorithms for
469 removing the shattered particles (Jackson and McFarquhar, 2014; Jackson et al., 2014). In
470 order to account for the anti-shattering effect, observed ice number concentrations were
471 scaled by a factor of 1/4 and 1/2, respectively, to consider the possible range of the
472 shattering effect. Furthermore, to be consistent with Figure 10 in Jackson et al. (2014), only
473 ice particles with diameters larger than 100 μm are included in our model, and observation
474 intercomparisons.

删除了: ←

删除了: the

删除了: was

删除了: and shown

删除了: -

475 3.3 Model set up and description of model experiments

476 In this study, we run SCAM with 32 vertical layers from the surface up to 3 hPa. The
477 model is initialized and driven by the large-scale forcing data at every 3 hours. The forcing
478 data developed by Xie et al. (2006) include the divergences and advections of moisture and
479 temperature as well as the surface flux. The simulation period is from 5 to 22 October 2004
480 and covers the second and third synoptic regimes and the transition period between them.

删除了: which were

删除了: The model is driven by the large-scale forcing data every 3 hours, which were developed based on Xie et al. (2006)...

481 A detailed description of model experiments along with SIP mechanisms in these
482 experiments is provided in Table 1. The control experiment (CTL) uses the default CAM6
483 model that only includes the SIP, due to the HM process. The impacts of two new SIP
484 mechanisms, including the ice-ice collision break-up and rain freezing fragmentation based
485 on Phillips et al. (2017a, 2018) are addressed in the SIP_PHIL experiment. To examine the

删除了: model

删除了: does not

删除了: s

删除了: ice-ice collision break-up and rain freezing fragmentation...

删除了: processes

501 impact of rime splintering in the CTL experiment, we conducted CTL_no_HM experiment
502 that is similar to CTL but without ~~the~~ HM process.

503

504 4 Results

505 4.1 SIP impacts on different types of clouds during M-PACE

506 Figure 4 shows the temporal evolution of LWP, IWP, and cloud fractions from two
507 model simulations (CTL and SIP_PHIL) and their comparison to observations. The model
508 simulations cover the second and third synoptic regimes as well as the transition period
509 between them. Two different types of clouds were formed in response to the strong surface
510 forcing during the second synoptic regime from 4 to 14 October. As shown in Fig. 4c,
511 multilayer stratus occurred from 5 to 8 October, and the clouds extended ~~from 950 hPa~~ up to
512 500 hPa. ~~Between 9 and 14 October, single-layer boundary layer stratus occurred between~~
513 ~~800 and 950 hPa.~~ Because of the dramatic change in cloud types in the second regime, we
514 further separate the second regime into two time periods. Then, we select typical days in the
515 four time periods for our analysis in this study, as shown in Fig. 4. The period from 6 to 8
516 October is selected as the “multilayer stratus” period. The period ~~from 9~~ to 12 October is
517 selected as the “single-layer stratus” period, followed by the transition period marked on 16

删除了: from 950 hPa

删除了: mixed-phase

删除了: -

删除了: between

522 October. The period between 18 and 20 October is selected to represent the “frontal cloud”
523 type during the third regime.

524 Figure 4 shows that the simulated IWP is systematically underestimated during M-
525 PACE in the CTL experiment. The maximum value of IWP in CTL is smaller than 50 g m^{-2}
526 ² during M-PACE, but up to 500 g m^{-2} in the measurements. The SIP_PHIL experiment
527 shows decreased LWP and increased IWP compared with CTL, reaching a better agreement
528 with the measurements. For example, IWP increases from 50 g m^{-2} in CTL to 425 g m^{-2} in
529 SIP_PHIL on 20 October, compared with $300 \sim 475 \text{ g m}^{-2}$ from different measurements (Fig.
530 4). The simulated LWP is overestimated during the “multilayer stratus”, the second half of
531 the “single-stratus”, and the “frontal cloud” periods in CTL, particularly on 20 October.
532 The SIP_PHIL experiment decreases the LWP from 550 g m^{-2} in CTL to 300 g m^{-2} on 11
533 October and from 425 g m^{-2} in CTL to 70 g m^{-2} on 20 October (Fig. 4a). The CTL no HM
534 experiment has similar results as the CTL experiment.

535 During the multilayer stratus period, the CTL and SIP_PHIL experiments show that the
536 cloud top is located at about 5 km with a temperature of $-20 \text{ }^\circ\text{C}$ (Fig. 5). These cloud
537 properties are consistent with the observations (Verlinde et al., 2007) that show a minimum
538 observed cloud temperature of -17°C (Fig. 4). However, we notice a significant
539 overestimation of cloud amount at 6–8 km on 7 October by the model simulations in Fig. 5,
540 as compared to the observation in Fig. 4c.

删除了: LWP is substantially overestimated during the second half of the single-stratus period. The SIP_PHIL experiment decreases the LWP from 425 g m^{-2} in CTL to 70 g m^{-2} on 20 October (Fig. 4a)

删除了: compared with

删除了: Multilayer stratus
T

删除了: during the multilayer stratus period,

删除了: at

删除了: s

删除了: ↵

552 During this period, IWC is increased in the SIP_PHIL experiment, compared to CTL,
553 while LWC is decreased. The mean vertical profiles of simulated IWC and LWC in this
554 period are shown in Fig. 6. The simulated values of LWC and IWC are lower than
555 observations, particularly for IWC. LWC decreases from 130 mg m^{-3} in CTL to 80 mg m^{-3}
556 in SIP_PHIL below 1 km. IWC increases from 3 mg m^{-3} in CTL to 5 mg m^{-3} in SIP_PHIL.
557 The time-averaged IWP increases from 11.2 g m^{-2} in CTL to 17.1 g m^{-2} in SIP_PHIL but is
558 still lower than the observed value of 55.6 g m^{-2} (Table 2). After considering the SIP in the
559 model, for the multilayer stratus period, ICNC is increased by 1 L^{-1} (Fig. 5) at an altitude of
560 1 to 4 km. Observations of ICNC are not available during this period.

561 Between 9 and 14 October, a persistent boundary-layer mixed-phase stratus occurred
562 between 800-950 hPa, with the cloud top temperature at around $-15 \text{ }^{\circ}\text{C}$ (Verlinde et al., 2007).
563 This single-layer stratus was separated from the surface based on the measurement (Fig. 4c).
564 However, modeled clouds extend to the surface in CTL (Fig. 5). This bias is alleviated in
565 SIP_PHIL, and the clouds are slightly decoupled from the surface on 8 and 11 October (Fig.
566 5). Previous studies also found that this bias partially results from the overestimation of low-
567 level moisture in the large-scale forcing data (Zhang et al., 2019, 2020).

568 Observed cloud liquid is located above the cloud ice during this period, with the LWC
569 peak $\sim 0.5 \text{ km}$ above the IWC peak. Observed vertical profile of LWC shows a maximum of
570 300 mg m^{-3} (ranging from 210 to 500 mg m^{-3}) at $\sim 1.25 \text{ km}$, while observed IWC is peaked
571 at 0.75 km (Fig. 6). This characteristic is clearly captured by the SIP_PHIL experiment, with

删除了: the multilayer stratus

删除了: simulation

删除了: liquid water content (

删除了:)

删除了: the multilayer stratus

删除了: .

删除了: ~~Boundary-layer mixed-phase stratus~~

删除了: ~~during~~

580 the peaks of LWC and IWC located at 0.75 and 0.5 km, respectively (Fig. 6). A better relative
581 position of cloud liquid and ice in SIP_PHIL indicates a better simulation of interactions
582 between cloud physics and dynamics. This distinct feature also contributes to the longevity
583 of mixed-phase clouds in the Arctic, as discussed in Section 1. In SIP_PHIL, the maximum
584 IWC value is four times larger than that in CTL (2 versus 0.5 mg m⁻³); accordingly,
585 temporally-averaged IWP increases from 0.9 in CTL to 2.5 g m⁻² in SIP_PHIL (Table 2).
586 Meanwhile, ICNC in SIP_PHIL is higher than that in CTL, and the maximum ICNC goes
587 up by 5 L⁻¹ at 0.5 km on 11 October (Fig. 5). Thus, SIP adds an extra source of ice crystals
588 to the boundary-layer mixed-phase stratus clouds.

589 During the transition period, several distinct liquid layers are interrupted by the ice
590 enriched layers in the observation. Due to the coarse vertical resolution, the model may not
591 be able to capture this vertical variation accurately. Considerable variation was noticed in the
592 observed IWC with a maximum IWC of 0.8–1.8 mg m⁻³ (Fig. 7). The CTL experiment
593 substantially underestimates IWC, as it produces IWC less than 0.1 mg m⁻³. The maximum
594 IWC in SIP_PHIL is 1.15 mg m⁻³, providing a better agreement with the observation. The
595 simulated peak LWC is decreased from 80 in CTL to 65 mg m⁻³ in SIP_PHIL, which is
596 closer to the observed value of 55 mg m⁻³. The temporally-averaged IWP in SIP_PHIL is
597 10⁴ times larger than that in CTL, with values of 0.0001, 3.6, and 5.6 g m⁻² in CTL, SIP_PHIL,
598 and observation, respectively (Table 2). The vertically-integrated ICNC is 7.66 and 4.57×10⁵

删除了: ↵

删除了: mean

删除了: <#>Transition period↵

删除了: <#>

删除了: <#> (Fig. 7)

删除了: <#>from

删除了: <#>from

606 L⁻¹ in CTL and SIP_PHIL, respectively (Table 2). Considering SIP in the model increases

607 ~~vertically~~ integrated ICNC by five orders of magnitude during the transition period.

608 During the frontal cloud period, ~~stratocumulus and altostratus clouds associated with~~
609 the frontal system extended from the surface up to 8 km (Fig. 4). ~~The SIP PHIL experiment~~

610 ~~shows the largest absolute increases in IWC and ICNC compared to the other periods (Fig.~~

611 ~~5).~~ The peak of modeled IWC is located at 2.5 km, with values of 2 and 8 mg m⁻³ in CTL

612 and SIP_PHIL, respectively (Fig. 7), much lower than the observation (ranging from 8 to 40

613 mg m⁻³). IWP is ~~10.4, 26.1, and 96~~ g m⁻² in CTL, SIP PHIL, ~~and the observation,~~

614 respectively (Table 2). ICNC is increased by up to 7 L⁻¹ between 2 to 4 km on 20 October

615 from CTL to SIP_PHIL (Fig. 5). ~~The simulated LWP is decreased from 127.6 to 41.2 g m⁻²,~~

616 which is closer to the observed value of 50.2 g m⁻².

617 The relative importance of primary and secondary ice production is shown as pie

618 charts in Fig. 8, to identify the dominant ice production mechanism in different types of

619 ~~the~~ Arctic clouds. The primary ice production (i.e., ice nucleation) is more important in the

620 clouds with colder cloud tops, such as multilayer stratus and frontal clouds with cloud top

621 temperatures colder than -25 °C and -40 °C, respectively. The primary ice production

622 contributes 37% and 69% to the total ice production during the multilayer stratus and

623 frontal cloud periods, respectively. Primary ice production is more efficient in deep clouds

624 due to the inverse relationship between the ice nucleation rate and temperature. SIP is more

625 important than primary ice production in the boundary-layer stratus and in clouds during

删除了: <#>column

删除了: <#>

删除了: <#>Frontal clouds⁴

删除了: <#>the SIP_PHIL experiment shows highest absolute increase in IWC and ICNC compared to the other periods. S

删除了: <#>(Verlinde et al., 2007)

删除了: <#>in the measurements and simulations

删除了: <#>5

删除了: <#>96,

删除了: <#>and

删除了: <#>the observation,

删除了: <#>and

删除了: <#>IWP and ICNC in SIP_PHIL are about two times of those in CTL.

删除了: <#>SIP versus primary ice production in different types of clouds⁴

643 the transition period when cloud top temperatures were at $-15\text{ }^{\circ}\text{C}$. The fragmentation of
644 freezing raindrops contributes the most (up to 80%) to the ice production in the single-layer
645 boundary-layer stratus. The break-up from ice-ice collisions contributes 22% to the total
646 ice production in the frontal clouds, while the rime splintering contributes 22% to the
647 multilayer stratus. These two SIP mechanisms (i.e., break-up from ice-ice collisions and
648 rime splintering) account for a small fraction of the ice production in the boundary-layer
649 stratus.

650 Next, we will focus on the SIP impacts on the boundary-layer stratus related to the
651 phase partitioning (section 4.2) and ICNC (section 4.3).

652 **4.2 SIP impact on occurrence and phase partitioning of the mixed-phase** 653 **clouds**

654 Figure 9 shows the liquid fraction (defined as $\text{LWC}/(\text{LWC}+\text{IWC})$) as a function of
655 normalized height in the single-layer boundary-layer stratus. The normalized height Z_n is 0
656 at cloud base and 1 at cloud top. IWC from the model includes all the ice hydrometeors to
657 compare it with observations. Fig. 9a reveals two features of the observed single-layer
658 boundary-layer clouds: (1) mixed-phase is dominant in the clouds, and (2) the liquid fraction
659 increases with cloud altitude. The liquid fraction is between 0.05 and 0.95 in most portions
660 of the clouds, indicating a mixed-phase feature in the observation. In the upper portion of the
661 clouds, observed liquid fraction is larger than 0.6 with the mean value increasing with height.

删除了: mixed-phase

删除了: mixed-phase

删除了: Measurements showed in

移动了(插入) [1]

删除了: The increase of ice mass fraction in the lower portion of the clouds results from the ice growth by riming of cloud liquid and ice sedimentation from the upper levels.

删除了: es

669 In the lower portion of the clouds ice mass fraction increases as a result of ice growth by
670 riming of cloud liquid and ice sedimentation from the upper levels. The CTL experiment
671 cannot reproduce the observed mixed-phase feature. A large portion of the clouds is in liquid
672 phase with the liquid fraction close to 1 in CTL, which significantly overestimates the liquid
673 fraction in the clouds. This is vastly different from previous versions of CAM. CAM5
674 showed an underestimation of the liquid fraction (Liu et al., 2011; [Cesana et al., 2015](#); [Tan](#)
675 [and Storelvmo, 2016](#); [Zhang et al., 2019](#); [Tan and Storelvmo, 2019](#)), while CAM3 showed
676 a decrease of the liquid fraction with height due to its use of a temperature-dependent phase
677 partitioning (Liu et al., 2007).

678 The SIP_PHIL experiment improves the model simulation of cloud phase with
679 increased ice fraction in the bottom half of the clouds by adding an extra source of ice crystals
680 from SIP, (Fig. 9c). The CTL no HM experiment gives very similar results as the CTL
681 experiment (Fig. 9d). Note that the modeled liquid fraction distributes on discrete vertical
682 levels (Fig. 9b, c, d) due to the coarse model vertical resolution (with only 10 vertical levels
683 below 2 km). In contrast, observed data were detected at 10 s⁻¹ resolution during spiral
684 ascents and descents in the clouds so that the observed liquid fraction is distributed
685 continuously with height.

686 For the cloud occurrence, 62.7% of observed clouds are mixed-phase, and only 16%
687 are liquid-phase during the single-layer stratus period, as shown in Table 3. The liquid phase
688 cloud occurrence is 73% in CTL and only 26.9% for mixed-phase clouds, indicating too

删除了: a

删除了: Note that the modeled liquid fraction distributes on discrete vertical levels (Fig. 9b, c) due to a coarse model vertical resolution (with only 10 vertical levels below 2 km). In contrast, observed data were detected at 10 s⁻¹ resolution during spiral ascents and descents in the clouds so that observed liquid fraction is distributed continuously with height. ...

删除了: with the liquid fraction varying between 0 to 1

上移了 [1]: The increase of ice mass fraction in the lower portion of the clouds results from the ice growth by riming of cloud liquid and ice sedimentation from the upper levels. In the upper portion of the clouds, observed liquid fraction is larger than 0.6 with the mean value increases with height.

删除了: better captures the mixed-phase feature in the bottom half of the clouds,

删除了: features "too much liquid and too little ice" in the mixed-phase clouds, while the SIP_PHIL experiment

删除了: improves the model simulation of cloud phase with increased ice fraction at lower altitudes by adding an extra source of ice crystals from SIP.

710 much liquid-phase and too less mixed-phase occurrence in CAM6. The mixed-phase cloud
 711 occurrence is 58.8% in SIP_PHIL and agrees much better with the observation. Thus, there
 712 are more frequent mixed-phase clouds in SIP_PHIL. ~~However, the occurrence of ice phase~~
 713 ~~is still underestimated and that of the liquid phase overestimated~~ in SIP_PHIL. Note that, we
 714 define the modeled clouds with total cloud water amount larger than 0.001 g m^{-3} and the
 715 liquid fraction between 0.5% and 99.5% as the mixed-phase clouds, which are consistent
 716 with the observation (McFarquhar et al., 2007).

- 删除了: ,
- 删除了: but
- 删除了: clouds
- 删除了: are
- 删除了: ↵

717 4.3 SIP impact on ice crystal number concentration

718 4.3.1 Vertical distribution of ice crystal number concentration

719 The vertical distribution of ICNCs in the single-layer boundary-layer ~~stratus~~ clouds
 720 on October 9, 10, and 11 from model simulations and observations is shown in Figure 10.
 721 The measured ICNCs ~~when applied with a correction factor of 1/4~~ range from ~~0.02~~ to ~~20~~ L^{-1}
 722 ~~1~~, with an average value of ~~1~~ L^{-1} . ~~The CTL and CTL_no_HM experiments have similar~~
 723 ~~results, and both underestimate the ICNCs in all the cloud layers, with a mean ICNC of~~
 724 ~~$\sim 0.1 \text{ L}^{-1}$ and the maximum concentration of 1 L^{-1}~~ . The mean ICNC is increased to ~~~ 1~~ L^{-1}
 725 in the SIP_PHIL experiment with ~~the~~ maximum concentration of ~~30~~ L^{-1} , which are in better
 726 agreement with the observations compared to CTL. ICNCs are increased by more than one

- 删除了: mixed-phase
- 删除了: Here, the ICNCs from the model only include ice particles with diameter larger than $53 \mu\text{m}$ to be consistent with the observed size limit for ice particles.
- 删除了: In single-layer mixed-phase clouds, t
- 删除了: d
- 删除了: 1
- 删除了: 100
- 删除了: 5
- 删除了: a
- 删除了: the two
- 删除了: experiments
- 删除了: The CTL experiment underestimates the ICNCs in all the cloud layers, with a mean ICNC of $\sim 0.25 \text{ L}^{-1}$ and the maximum concentration of 3 L^{-1}
- 删除了: 3
- 删除了: a
- 删除了: 10

750 order of magnitude in the lower portion of the clouds, although they are still lower than
751 those observed in the upper portion of the clouds.

752 Figure 10 also shows the linear regressions of ICNCs as a function of cloud altitude
753 (black lines). ICNCs increase towards the cloud base in the observation, revealing ice
754 multiplication during the ice growth and sedimentation. The CTL experiment shows that
755 the ICNCs decrease towards the cloud base, an opposite pattern compared to the
756 observation. SIP_PHIL captures the observed pattern in the vertical profile of ICNCs (Fig.
757 10c), suggesting that SIP is an important source of ice crystals near the cloud base in the
758 Arctic boundary-layer mixed-phase stratus. Furthermore, the vertical distribution of ice
759 particles is important for the longevity of the Arctic mixed-phase clouds, which features
760 lower ICNCs in the upper portion of clouds and higher ICNCs towards the cloud base.

761 4.3.2 PDF of ice crystal number concentration

762 Figure 11 shows the probability density function (PDF) (i.e., the frequency of
763 occurrence) of ICNCs from model simulations and observations for the boundary-layer
764 mixed-phase stratus period (October 9-12, 2004). Note that only particles with a diameter
765 greater than 100 μm are included in the observed and modeled ICNCs. The PDF
766 distribution in SIP_PHIL shows a shift to the right, with the ICNC peak much closer to the
767 observations than CTL. The median ICNC is 0.13 L^{-1} in CTL, shifting to 0.27 L^{-1} in
768 SIP_PHIL, which is closer to the observed median value of 0.32 L^{-1} .

删除了: The

删除了: s

删除了: s

删除了: The

删除了: is well captured in SIP_PHIL

删除了: 53

删除了: 26

删除了: 48

删除了: 1.27

778 The PDF distribution in SIP_PHIL also has a broader distribution than CTL. A
 779 broader distribution indicates that the maximum concentrations are higher in the
 780 observation and SIP_PHIL compared to CTL. In the CTL experiment, the frequency of
 781 occurrence of ICNCs is much lower (higher) than observations when their values are higher
 782 (lower) than 0.1 L^{-1} . These biases in ICNCs PDF are much improved in SIP_PHIL, leading
 783 to a better agreement with the observation. The frequency occurrence of ICNC at 1 L^{-1} is
 784 2.12%, 10.37%, 13.77% in CTL, SIP_PHIL, and observation, respectively. Thus,
 785 SIP_PHIL has an occurrence frequency of ICNC larger than 1 L^{-1} , which is 5 times of that
 786 in CTL. We note that the agreement between modeled and observed ICNCs is improved
 787 with a correction factor of $\frac{1}{4}$ (Figures 10 and 11) and a correction factor of $\frac{1}{2}$
 788 (supplementary Figures S2 and S4) to the observed ICNCs, compared to that without a
 789 correction factor (Supplementary Figures S1 and S3). This is because model simulations
 790 including SIP_PHIL underestimate the observed ICNCs without the correction of the
 791 shattering effect.

792 **4.3.3 Dependence of ice enhancement on cloud temperature**

793 The bivariate joint PDF defined in terms of temperature and ice enhancement
 794 ($N_{\text{SIP_PHIL}}/N_{\text{CTL}}$) during the M-PACE is shown in Fig. S5. Strong ice enhancements are
 795 noticed at temperatures from -3 to -16°C , and ICNCs are increased by nearly 4 orders of
 796 magnitude in SIP_PHIL compared with CTL. As temperature decreases below -35°C , ice

- 删除了: 5
- 删除了: 0.5
- 删除了: 1.5
- 删除了: 1.5
- 删除了: 3
- 删除了: observed and
- 删除了: ice number concentrations
- 删除了: ,
- 删除了: as shown in
- 删除了:
- 删除了: with a correction factor of $\frac{1}{4}$
- 删除了: in
- 删除了: with a correction factor of $\frac{1}{2}$
- 删除了: the
- 删除了: all
- 删除了: the
- 删除了: ice number concentrations
- 删除了: Figure 12 shows t
- 删除了: is

816 enhancement happens again, but with a reduced magnitude. For example, the largest
817 enhancement at -44°C is around 3.2, with a frequency of 1% to 7%.

818 To investigate the dominant processes that contribute to the strong enhancement
819 near -10°C we plotted the bivariate joint PDF defined in terms of temperature and ice
820 production rate (Fig. 12). A clear relationship between ice enhancement and fragmentation
821 of freezing raindrops can be seen at temperatures from -20 to -4°C in Fig. 12 and Fig. S5.
822 The maximum ice production from the fragmentation of freezing raindrops is 160 L^{-1} (i.e.,
823 $10^{2.2}$) at temperatures ranging from -8 to -14°C . Even though rime splintering also
824 happens at temperatures between -8 to -3°C with a maximum value of 20 L^{-1} , its ice
825 production is almost one order of magnitude lower than that from the fragmentation of
826 freezing raindrops. Between -20 to -16°C , primary ice nucleation and fragmentation of
827 freezing raindrops coexist, with the fragmentation of freezing raindrops more efficient
828 (with a magnitude of 10 L^{-1}) comparing to the primary ice nucleation (about 1 L^{-1}). Primary
829 ice nucleation has the largest production of up to 250 L^{-1} at temperatures ranging from $-$
830 32 to -25°C . Below -35°C , ice-ice collision break-up frequently happens, but with a lower
831 process rate.

832 In summary, the strongest ice enhancement occurs in the moderately supercooled
833 clouds with temperatures around -10°C . ICNCs are increased by up to 4 orders of
834 magnitude mainly from the fragmentation of freezing raindrops. A weaker ice

删除了: 3

删除了: s

删除了: 1

删除了: 3

删除了: it

删除了: increases

删除了: arising

842 enhancement is noticed frequently in ice clouds with temperatures below -35°C , which is
843 attributed to the ice-ice collision break-up.

844 5 Summary, conclusions and outlook

845 In this study, two new SIP mechanisms are implemented in a GCM model (CAM6)
846 to investigate their impacts on the Arctic mixed-phase clouds, which were observed during
847 the DOE ARM M-PACE field campaign. The CAM6 model with the new SIP provides a
848 better simulation of the distinct “liquid cloud top, ice cloud base” feature of long-lived
849 Arctic boundary-layer mixed-phase clouds.

850 We find that model biases of underestimation of mixed-phase cloud occurrence and
851 overestimation of pure liquid cloud occurrence are reduced for the single-layer stratus after
852 considering the new SIP processes. The mixed-phase cloud occurrence is 26.9%, 58.8%, and
853 62.7% in CTL, SIP_PHIL and the observation, respectively, while the pure liquid cloud
854 occurrence is reduced from 73% in CTL to 40% in SIP_PHIL, in a better agreement with
855 observed 16%.

856 We find that the pattern of the vertical distribution of ICNCs in the single-layer
857 stratus is reversed after considering the new SIP processes in the model. The measured
858 decrease of ICNCs with cloud height is captured by SIP_PHIL but not by CTL. SIP also
859 leads to a shift of PDF of ICNCs towards a more frequent occurrence of high ICNCs and

删除了: multiple

861 a less frequent occurrence of low ICNCs. We notice a taller PDF with higher peak and a
862 broader tail in SIP_PHIL, indicating that high ICNCs occur more frequently with the
863 occurrence of extreme high ICNCs ($>10^2 \text{ L}^{-1}$) in SIP_PHIL, which is absent in CTL.

864 The maximum ICNC is around 1, 30, and 20 L^{-1} in CTL, SIP PHIL, and
865 observation, respectively, in the single-layer stratus. During the frontal cloud period, the
866 SIP_PHIL experiment shows the largest absolute increases in IWC and ICNC by 6 mg m^{-3}
867 and 7 L^{-1} , respectively. The largest ice enhancement ($N_{\text{SIP_PHIL}}/N_{\text{CTL}}$) is noticed during the
868 transition period with a moderately cold cloud top temperature. The column integrated ICNC
869 increases by five orders of magnitude and IWP increases by four orders of magnitude in
870 SIP_PHIL compared to CTL. When comparing the relative importance between primary
871 and secondary ice production, we notice that primary ice nucleation is more dominant in
872 the deep clouds with cloud tops reaching up to 10 km. At the same time, the fragmentation
873 of freezing raindrops contributes more to ICNCs in the boundary-layer clouds.

874 At temperatures from -4 to -20 $^{\circ}\text{C}$, significant ice enhancement is attributed to the
875 fragmentation of freezing raindrops, with the maximum ice production of 160 L^{-1} at -10 $^{\circ}\text{C}$.
876 A weaker ice enhancement due to ice-ice collision break-up is noticed in ice clouds with
877 temperatures below -35 $^{\circ}\text{C}$ but with unneglectable occurrence frequencies. Primary ice
878 nucleation has the largest production by up to 251 L^{-1} in the relatively cold-mixed phase
879 clouds with temperatures between -32 to -25 $^{\circ}\text{C}$.

删除了: 3

删除了: 100

删除了: 100

删除了: mixed-phase clouds

删除了: The ice enhancement from SIP is strongest in moderately supercooled temperatures around -10 $^{\circ}\text{C}$. ICNCs increase by up to 4 orders of magnitude. A weaker ice enhancement is noticed at ice clouds with temperatures below -35 $^{\circ}\text{C}$, with a small, enhanced magnitude but unneglectable occurrence frequencies.

删除了: ranging

删除了: s

删除了: value

893 In summary, the consideration of the new SIP processes in CAM6 results in a
894 significant improvement in the model simulated clouds during M-PACE. It underscores
895 the critical role of SIP in cloud microphysics, which should be considered in the
896 parameterizations of GCMs.

删除了: mixed-phase

897 In this study, the parameterization of the HM process rate is based on Cotton et al.
898 (1986). In this parameterization the ice production rate does not have a dependence on
899 droplet size. Lacking the effect of cloud droplet spectrum in the HM process is supposed to
900 result in an overestimated splintering rate in the Arctic clouds, especially for the clouds with
901 cloud-bases close to the freezing level and with small droplets in the clouds. However, the
902 overestimation in the HM splintering rate due to lack of the cloud droplet spectrum might be
903 balanced by neglecting the raindrop splintering in the HM process in the MG microphysics.
904 In this study, we keep using the bulk approach to represent the HM process, to be the same
905 as that in the standard MG microphysics scheme. It would be interesting to examine the
906 impact of a bin approach to represent the HM process on modeled clouds, which will be a
907 topic of our future studies.

删除了: ↵

删除了: Future work should also explore potential impacts of the graupel related SIP processes, and potential interactions of primary ice nucleation with SIP to impact cloud features.

删除了: ,

删除了: i

908 For the ice fragmentation from ice-ice collisions, the graupel related collisions are
909 not included in this study, because the current MG microphysical scheme does not treat
910 graupel. To quantify the impacts of graupel on SIP, the cloud microphysical scheme with
911 prognostic graupel (Gettelman et al., 2019) or a “Single-Ice” microphysical scheme
912 (Morrison and Milbrandt, 2015; Zhao et al., 2017) will be needed.

删除了: However, it was found that this process rate also depends on the cloud droplet spectrum (Mossop, 1978; Phillips et al., 2001), in addition to temperature and the riming rate. Lacking the effect of cloud droplet spectrum in HM process is supposed to result in an overestimated splintering rate in the Arctic clouds, especially for the clouds which cloud-base is close to the freezing level and have small droplets in the cloud.

删除了: cloud

删除了: currently

删除了: to further examine the impacts of graupel

931 We note that the representation of ice properties is highly simplified in the current
932 model. Firstly, ice particles in nature are featured with continuous size distributions with
933 complex shapes and a wide range of densities. In contrast, the current model artificially
934 classifies them into two categories (i.e., cloud ice and snow) with fixed densities, e.g.,
935 densities of 500 kg m⁻³ for cloud ice and of 250 kg m⁻³ for snow. Moreover, the shape of
936 all ice particles is assumed to be spherical. The parameters, *a* and *b* in the relationship of
937 terminal velocity and diameter ($V-D$, $V=aD^b$) are fixed values for cloud ice and snow.
938 These assumptions cannot represent the complexities of ice properties (e.g., size
939 distribution, density, shape, and fall speed) in the measurement. Lastly, the riming intensity
940 of ice particles changes as ice collides with supercooled liquid, leading to significant
941 changes in density and fall speed of ice. This evolution of ice properties is currently not
942 represented in the model. A promising method is to represent the ice-phase microphysics
943 with varying ice properties (Morrison and Milbrandt, 2015; Zhao et al., 2017).

删除了: Furthermore,

删除了:

删除了: of all

删除了: Furthermore

删除了: ↵

944

945 **Competing interests:** The authors declare that they have no conflict of interest.

946

947 **Data availability:** The model code is available at <https://github.com/CESM-Development>.

948 The observation data of M-PACE campaign is obtained from the Atmospheric Radiation

949 Measurement (ARM) user facility, a U.S. Department of Energy Office of Science,

950 available at <https://www.arm.gov/research/campaigns/nsa2004arcticclld>.

956

957 **Author contributions:** XZ and XL conceptualized the analysis and wrote the manuscript
958 with input from the co-authors. XZ modified the code, carried out the simulations, and
959 performed the analysis. VP and SP provided the model code for the secondary ice
960 production. VP and SP also provided scientific suggestions to the manuscript. XL was
961 involved with obtaining the project grant and supervised the study. All authors were
962 involved in helpful discussions and contributed to the manuscript.

963

964 **Acknowledgment:** This research was supported by the DOE Atmospheric System
965 Research (ASR) Program (grant DE-SC0020510). We thank Meng Zhang for helpful
966 discussions especially on processing the observation data. [We thank Dr. Chuanfeng Zhao](#)
967 [and Dr. Greg McFarquhar for their](#) suggestions on processing the observation data.

968

969 **Reference**

- 970 Bennartz, R., Shupe, M. D., Turner, D. D., Walden, V. P., Steffen, K., Cox, C. J., Kulie,
971 M. S., Miller, N. B., and Pettersen, C.: July 2012 Greenland melt extent enhanced by
972 low-level liquid clouds, *Nature*, 496, 83-86, 10.1038/nature12002, 2013.
- 973 Cesana, G., and Chepfer, H.: Evaluation of the cloud thermodynamic phase in a climate
974 model using CALIPSO-GOCCP, *Journal of Geophysical Research Atmospheres*,
975 118, 7922-7937, 10.1002/jgrd.50376, 2013.
- 976 Cesana, G., Waliser, D. E., Jiang, X., and Li, J. L. F.: Multimodel evaluation of cloud
977 phase transition using satellite and reanalysis data, *Journal of Geophysical Research:*
978 *Atmospheres*, 120, 7871-7892, 10.1002/2014JD022932, 2015.
- 979 Connolly, P. J., Heymsfield, A. J., and Choullarton, T. W.: Modelling the influence of
980 rimer surface temperature on the glaciation of intense thunderstorms: The rime-
981 splinter mechanism of ice multiplication, *Q J Roy Meteor Soc*, 132, 3059-3077,
982 10.1256/qj.05.45, 2006.
- 983 Cotton, W. R., Tripoli, G. J., Rauber, R. M., and Mulvihill, E. A.: Numerical Simulation
984 of the Effects of Varying Ice Crystal Nucleation Rates and Aggregation Processes
985 on Orographic Snowfall, *American Meteorological Society*, 1658-1680, 1986.
- 986 Dearden, C., Vaughan, G., Tsai, T., and Chen, J. P.: Exploring the diabatic role of ice
987 microphysical processes in two north atlantic summer cyclones, *Mon Weather Rev*,
988 144, 1249-1272, 10.1175/MWR-D-15-0253.1, 2016.
- 989 Deng, M., and Mace, G. G.: Cirrus microphysical properties and air motion statistics
990 using cloud radar Doppler moments. Part I: Algorithm description, *J Appl Meteorol*
991 *Clim*, 45, 1690-1709, 10.1175/JAM2433.1, 2006.
- 992 Dong, X., and Mace, G. G.: Profiles of low-level stratus cloud microphysics deduced
993 from ground-based measurements, *J Atmos Ocean Tech*, 20, 42-53, 10.1175/1520-
994 0426(2003)020<0042:POLLSC>2.0.CO;2, 2003.
- 995 Feingold, G., Walko, R. L., Stevens, B., and Cotton, W. R.: Simulations of marine
996 stratocumulus using a new microphysical parameterization scheme, *Atmospheric*
997 *Research*, 47-48, 505-528, 10.1016/S0169-8095(98)00058-1, 1998.
- 998 Field, P. R., Lawson, R. P., Brown, P. R. A., Lloyd, G., Westbrook, C., Moisseev, D.,
999 Miltenberger, A., Nenes, A., Blyth, A., Choullarton, T., Connolly, P., Buehl, J.,
1000 Crosier, J., Cui, Z., Dearden, C., DeMott, P., Flossmann, A., Heymsfield, A., Huang,
1001 Y., Kalesse, H., Kanji, Z. A., Korolev, A., Kirchgaessner, A., Lasher-Trapp, S.,
1002 Leisner, T., McFarquhar, G., Phillips, V., Stith, J., and Sullivan, S.: Chapter 7.
1003 Secondary Ice Production - current state of the science and recommendations for the
1004 future, *Meteorological Monographs*, 58, 7.1-7.20, 10.1175/amsmonographs-d-16-
1005 0014.1, 2016.

1006 Fu, S., Deng, X., Shupe, M. D., and Xue, H.: A modelling study of the continuous ice
1007 formation in an autumnal Arctic mixed-phase cloud case, *Atmospheric Research*,
1008 228, 77-85, 10.1016/j.atmosres.2019.05.021, 2019.

1009 Gettelman, A. and Morrison, H.: Advanced two-moment bulk microphysics for global
1010 models. Part I: Off-line tests and comparison with other schemes, *Journal of*
1011 *Climate*, 28(3), 1268–1287, <https://doi.org/10.1175/JCLI-D-14-00102.1>, 2015.

1012 Gettelman, A., Morrison, H., Thayer-Calder, K., and Zarzycki, C. M.: The Impact of
1013 Rimed Ice Hydrometeors on Global and Regional Climate, *Journal of Advances in*
1014 *Modeling Earth Systems*, 11, 1543-1562, 10.1029/2018MS001488, 2019.

1015 Golaz, J. C., Larson, V. E., and Cotton, W. R.: A PDF-based model for boundary layer
1016 clouds. Part I: Method and model description, *Journal of the Atmospheric Sciences*,
1017 59, 3540-3551, 10.1175/1520-0469(2002)059<3540:APBMFB>2.0.CO;2, 2002.

1018 Grabowski, W. W., Thouron, O., Pinty, J. P., and Brenguier, J. L.: A hybrid bulk-bin
1019 approach to model warm-rain processes, *Journal of the Atmospheric Sciences*, 67,
1020 385-399, 10.1175/2009JAS3155.1, 2010.

1021 Intrieri, J. M., Shupe, M. D., Uttal, T., and McCarty, B. J.: An annual cycle of Arctic
1022 cloud characteristics observed by radar and lidar at SHEBA, *Journal of Geophysical*
1023 *Research: Oceans*, 107, SHE 5-1, 10.1029/2000jc000423, 2002.

1024 Jackson, R. C., and McFarquhar, G. M.: An assessment of the impact of antishattering
1025 tips and artifact removal techniques on bulk cloud ice microphysical and optical
1026 properties measured by the 2D cloud probe, *J Atmos Ocean Tech*, 31, 2131-2144,
1027 10.1175/JTECH-D-14-00018.1, 2014.

1028 Jackson, R. C., McFarquhar, G. M., Stith, J., Beals, M., Shaw, R. A., Jensen, J., Fugal, J.,
1029 and Korolev, A.: An assessment of the impact of antishattering tips and artifact
1030 removal techniques on cloud ice size distributions measured by the 2D cloud probe,
1031 *J Atmos Ocean Tech*, 31, 2567-2590, 10.1175/JTECH-D-13-00239.1, 2014.

1032 Jiang, H., Cotton, W. R., Pinto, J. O., Curry, J. A. and Weissbluth, M. J.: Cloud resolving
1033 simulations of mixed-phase Arctic stratus observed during BASE: Sensitivity to
1034 concentration of ice crystals and large-scale heat and moisture advection, *Journal of*
1035 *the Atmospheric Sciences*, 57(13), 2105–2117, [https://doi.org/10.1175/1520-](https://doi.org/10.1175/1520-0469(2000)057<2105:CRSOMP>2.0.CO;2)
1036 [0469\(2000\)057<2105:CRSOMP>2.0.CO;2](https://doi.org/10.1175/1520-0469(2000)057<2105:CRSOMP>2.0.CO;2), 2000.

1037 Kay, J. E. and Gettelman, A.: Cloud influence on and response to seasonal Arctic sea ice
1038 loss, *Journal of Geophysical Research*, 114(D18), D18204,
1039 <https://doi.org/10.1029/2009JD011773>, 2009.

1040 Khanal, S., and Wang, Z.: Evaluation of the lidar-radar cloud ice water content retrievals
1041 using collocated in situ measurements, *J Appl Meteorol Clim*, 54, 2087-2097,
1042 10.1175/JAMC-D-15-0040.1, 2015.

1043 Korolev, A. and Field, P. R.: The effect of dynamics on mixed-phase clouds: Theoretical
1044 considerations, *Journal of the Atmospheric Sciences*, 65(1), 66–86,
1045 <https://doi.org/10.1175/2007JAS2355.1>, 2008.

1046 Kuba, N., and Murakami, M.: Effect of hygroscopic seeding on warm rain clouds –
1047 numerical study using a hybrid cloud microphysical model, *Atmos Chem Phys*, 10,
1048 3335-3351, 10.5194/acp-10-3335-2010, 2010.

1049 Larson, V. E., Golaz, J.-C., and Cotton, W. R.: Small-Scale and Mesoscale Variability in
1050 Cloudy Boundary Layers: Joint Probability Density Functions, *Journal of the*
1051 *Atmospheric Sciences*, 59, 3519-3539, 10.1175/1520-
1052 0469(2002)059<3519:SSAMVI>2.0.CO;2, 2002.

1053 Liu, X., Easter, R. C., Ghan, S. J., Zaveri, R., Rasch, P., Shi, X., Lamarque, J. F.,
1054 Gettelman, A., Morrison, H., Vitt, F., Conley, A., Park, S., Neale, R., Hannay, C.,
1055 Ekman, A. M. L., Hess, P., Mahowald, N., Collins, W., Iacono, M. J., Bretherton, C.
1056 S., Flanner, M. G., and Mitchell, D.: Toward a minimal representation of aerosols in
1057 climate models: description and evaluation in the Community Atmosphere Model
1058 CAM5, *Geosci Model Dev*, 5, 709-739, 2012.

1059 Liu, X., Ma, P. L., Wang, H., Tilmes, S., Singh, B., Easter, R. C., Ghan, S. J., and Rasch,
1060 P. J.: Description and evaluation of a new four-mode version of the Modal Aerosol
1061 Module (MAM4) within version 5.3 of the Community Atmosphere Model, *Geosci*
1062 *Model Dev*, 9, 505-522, 2016.

1063 Liu, X., and Penner, J. E.: Ice nucleation parameterization for global models,
1064 *Meteorologische Zeitschrift*, 499-514, 10.1127/0941-2948/2005/0059, 2005.

1065 Liu, X., Xie, S., Boyle, J., Klein, S. A., Shi, X., Wang, Z., Lin, W., Ghan, S. J., Earle, M.,
1066 Liu, P. S. K. and Zelenyuk, A.: Testing cloud microphysics parameterizations in
1067 NCAR CAM5 with ISDAC and M-PACE observations, *Journal of Geophysical*
1068 *Research*, 116(24), D00T11, <https://doi.org/10.1029/2011JD015889>, 2011.

1069 Liu, X., Xie, S. and Ghan, S. J.: Evaluation of a new mixed-phase cloud microphysics
1070 parameterization with CAM3 single-column model and M-PACE observations,
1071 *Geophysical Research Letters*, 34(23), L23712,
1072 <https://doi.org/10.1029/2007GL031446>, 2007.

1073 McFarquhar, G. M., Zhang, G., Poellot, M. R., Kok, G. L., McCoy, R., Tooman, T.,
1074 Fridlind, A. and Heymsfield, A. J.: Ice properties of single-layer stratocumulus
1075 during the Mixed-Phase Arctic Cloud Experiment: 1. Observations, *Journal of*
1076 *Geophysical Research*, 112(D24), D24201, <https://doi.org/10.1029/2007JD008633>,
1077 2007.

1078 Morrison, H., de Boer, G., Feingold, G., Harrington, J., Shupe, M. D. and Sulia, K.:
1079 Resilience of persistent Arctic mixed-phase clouds, *Nature Geoscience*, 5(1), 11–17,
1080 <https://doi.org/10.1038/ngeo1332>, 2012.

1081 Morrison, H., and Milbrandt, J. A.: Parameterization of cloud microphysics based on the
1082 prediction of bulk ice particle properties. Part I: Scheme description and idealized
1083 tests, *Journal of the Atmospheric Sciences*, 72, 287-311, 10.1175/JAS-D-14-0065.1,
1084 2015.

1085 Mossop, S. C.: The influence of drop size distribution on the production of secondary ice
1086 particles during graupel growth, *Q J Roy Meteor Soc*, 104, 323-330,
1087 10.1002/qj.49710444007, 1978.

1088 Onishi, R., and Takahashi, K.: A warm-bin-cold-bulk hybrid cloud microphysical model,
1089 *Journal of the Atmospheric Sciences*, 69, 1474-1497, 10.1175/JAS-D-11-0166.1,
1090 2012.

1091 Phillips, V. T. J., Blyth, A. M., Brown, P. R. A., Choullarton, T. W., and Latham, J.: The
1092 glaciation of a cumulus cloud over New Mexico, *Q J Roy Meteor Soc*, 127, 1513-
1093 1534, 10.1002/qj.49712757503, 2001.

1094 Phillips, V. T. J., Patade, S., Gutierrez, J., and Bansemer, A.: Secondary ice production
1095 by fragmentation of freezing drops: Formulation and theory, *Journal of the*
1096 *Atmospheric Sciences*, 75, 3031-3070, 10.1175/JAS-D-17-0190.1, 2018.

1097 Phillips, V. T. J., Yano, J. I., Formenton, M., Ilotoviz, E., Kanawade, V., Kudzotsa, I.,
1098 Sun, J., Bansemer, A., Detwiler, A. G., Khain, A., and Tessendorf, S. A.: Ice
1099 multiplication by breakup in ice-ice collisions. Part II: Numerical simulations,
1100 *Journal of the Atmospheric Sciences*, 74, 2789-2811, 10.1175/JAS-D-16-0223.1,
1101 2017.

1102 Phillips, V. T. J., Yano, J. I., and Khain, A.: Ice multiplication by breakup in ice-ice
1103 collisions. Part I: Theoretical formulation, *Journal of the Atmospheric Sciences*, 74,
1104 1705-1719, 10.1175/JAS-D-16-0224.1, 2017.

1105 Pinto, J. O.: Autumnal mixed-phase cloudy boundary layers in the arctic, *Journal of the*
1106 *Atmospheric Sciences*, 55(11), 2016–2038, [https://doi.org/10.1175/1520-
1107 0469\(1998\)055<2016:AMPCBL>2.0.CO;2](https://doi.org/10.1175/1520-0469(1998)055<2016:AMPCBL>2.0.CO;2), 1998.

1108 Schwarzenboeck, A., Shcherbakov, V., Lefevre, R., Gayet, J. F., Pointin, Y., and
1109 Duroure, C.: Indications for stellar-crystal fragmentation in Arctic clouds,
1110 *Atmospheric Research*, 92, 220-228, 10.1016/j.atmosres.2008.10.002, 2009.

1111 Shupe, M. D. and Intrieri, J. M.: Cloud radiative forcing of the Arctic surface: The
1112 influence of cloud properties, surface albedo, and solar zenith angle, *Journal of*
1113 *Climate*, 17(3), 616–628, [https://doi.org/10.1175/1520-
1114 0442\(2004\)017<0616:CRFOTA>2.0.CO;2](https://doi.org/10.1175/1520-0442(2004)017<0616:CRFOTA>2.0.CO;2), 2004.

1115 Shupe, M. D., Matrosov, S. Y., and Uttal, T.: Arctic mixed-phase cloud properties
1116 derived from surface-based sensors at SHEBA, *Journal of the Atmospheric*
1117 *Sciences*, 63, 697-711, 10.1175/JAS3659.1, 2006.

1118 Shupe, M. D., Uttal, T., and Matrosov, S. Y.: Arctic cloud microphysics retrievals from
 1119 surface-based remote sensors at SHEBA, *J Appl Meteorol*, 44, 1544-1562,
 1120 10.1175/JAM2297.1, 2005.

1121 Sotiropoulou, G., Sullivan, S., Savre, J., Lloyd, G., Lachlan-Cope, T., Ekman, A. M. L.,
 1122 and Nenes, A.: The impact of secondary ice production on Arctic stratocumulus,
 1123 *Atmos Chem Phys*, 20, 1301-1316, 10.5194/acp-20-1301-2020, 2020.

1124 Sotiropoulou, G., Vignon, E., Young, G., Morrison, H., O'Shea, S., Lachlan-Cope, T.,
 1125 Berne, A., and Nenes, A.: Secondary ice production in summer clouds over the
 1126 Antarctic coast: an underappreciated process in atmospheric models, *Atmos Chem*
 1127 *Phys*, 1-30, 10.5194/acp-2020-328, 2020.

1128 Sullivan, S. C., Barthlott, C., Crosier, J., Zhukov, I., Nenes, A., and Hoose, C.: The effect
 1129 of secondary ice production parameterization on the simulation of a cold frontal
 1130 rainband, *Atmos Chem Phys*, 18, 16461-16480, 10.5194/acp-18-16461-2018, 2018.

1131 Sullivan, S. C., Hoose, C., Kiselev, A., Leisner, T., and Nenes, A.: Initiation of secondary
 1132 ice production in clouds, *Atmos Chem Phys*, 18, 1593-1610, 10.5194/acp-18-1593-
 1133 2018, 2018.

1134 Sullivan, S. C., Hoose, C., and Nenes, A.: Investigating the contribution of secondary ice
 1135 production to in-cloud ice crystal numbers, *Journal of Geophysical Research:*
 1136 *Atmospheres*, 122, 9391-9412, 10.1002/2017JD026546, 2017.

1137 Tan, I., and Storelvmo, T.: Sensitivity study on the influence of cloud microphysical
 1138 parameters on mixed-phase cloud thermodynamic phase partitioning in CAM5,
 1139 *Journal of the Atmospheric Sciences*, 73, 709-728, 10.1175/JAS-D-15-0152.1, 2016.

1140 Tan, I., and Storelvmo, T.: Evidence of Strong Contributions From Mixed-Phase Clouds
 1141 to Arctic Climate Change, *Geophys Res Lett*, 46, 2894-2902,
 1142 10.1029/2018GL081871, 2019.

1143 Turner, D. D., Clough, S. A., Liljegren, J. C., Clothiaux, E. E., Cady-Pereira, K. E., and
 1144 Gaustad, K. L.: Retrieving liquid water path and precipitable water vapor from the
 1145 atmospheric radiation measurement (ARM) microwave radiometers, 3680-3689,
 1146 [2007](#).

1147 Vavrus, S.: The impact of cloud feedbacks on Arctic climate under Greenhouse forcing,
 1148 *Journal of Climate*, 17, 603-615, 10.1175/1520-
 1149 0442(2004)017<0603:TIOCFO>2.0.CO;2, 2004.

1150 Verlinde, J., Harrington, J. Y., McFarquhar, G. M., Yannuzzi, V. T., Avramov, A.,
 1151 Greenberg, S., Johnson, N., Zhang, G., Poellot, M. R., Mather, J. H., Turner, D. D.,
 1152 Eloranta, E. W., Zak, B. D., Prenni, A. J., Daniel, J. S., Kok, G. L., Tobin, D. C.,
 1153 Holz, R., Sassen, K., Spangenberg, D., Minnis, P., Tooman, T. P., Ivey, M. D.,
 1154 Richardson, S. J., Bahrmann, C. P., Shupe, M., DeMott, P. J., Heymsfield, A. J., and
 1155 Schofield, R.: The mixed-phase arctic cloud experiment, *B Am Meteorol Soc*, 88,
 1156 205-221, 10.1175/BAMS-88-2-205, 2007.

1157 Wang, Y., Liu, X., Hoose, C., and Wang, B.: Different contact angle distributions for
1158 heterogeneous ice nucleation in the Community Atmospheric Model version 5,
1159 Atmos Chem Phys, 14, 10411-10430, 2014.

1160 Wang, Z.: A refined two-channel microwave radiometer liquid water path retrieval for
1161 cold regions by using multiple-sensor measurements, Ieee Geosci Remote S, 4, 591-
1162 595, 10.1109/LGRS.2007.900752, 2007.

1163 Wang, Z., and Sassen, K.: Cirrus cloud microphysical property retrieval using lidar and
1164 radar measurements. Part I: Algorithm description and comparison with in situ data,
1165 J Appl Meteorol, 41, 218-229, 10.1175/1520-
1166 0450(2002)041<0218:CCMPRU>2.0.CO;2, 2002.

1167 Xie, S., Boyle, J., Klein, S. A., Liu, X., and Ghan, S.: Simulations of Arctic mixed-phase
1168 clouds in forecasts with CAM3 and AM2 for M-PACE, Journal of Geophysical
1169 Research, 113, D04211-D04211, 10.1029/2007JD009225, 2008.

1170 Xie, S., Klein, S. A., Yio, J. J., Beljaars, A. C. M., Long, C. N., and Zhang, M.: An
1171 assessment of ECMWF analyses and model forecasts over the North Slope of
1172 Alaska using observations from the ARM Mixed-Phase Arctic Cloud Experiment,
1173 Journal of Geophysical Research, 111, D05107-D05107, 10.1029/2005JD006509,
1174 2006.

1175 Xie, S., McCoy, R. B., Klein, S. A., Cederwall, R. T., Wiscombe, W. J., Clothiaux, E. E.,
1176 Gaustad, K. L., Golaz, J. C., Hall, S. D., Jensen, M. P., Johnson, K. L., Lin, Y.,
1177 Long, C. N., Mather, J. H., McCord, R. A., McFarlane, S. A., Palanisamy, G., Shi,
1178 Y., and Turner, D. D.: ARM climate modeling best estimate data: A new data
1179 product for climate studies, B Am Meteorol Soc, 91, 13-20,
1180 10.1175/2009BAMS2891.1, 2010.

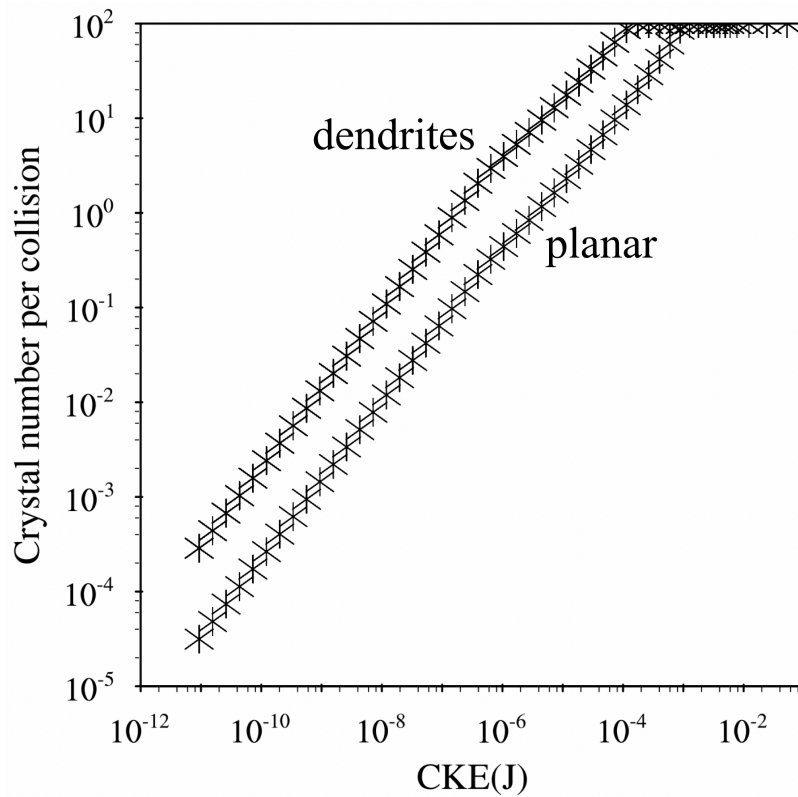
1181 Zhang, M., Liu, X., Diao, M., D'Alessandro, J. J., Wang, Y., Wu, C., Zhang, D., Wang,
1182 Z., and Xie, S.: Impacts of Representing Heterogeneous Distribution of Cloud
1183 Liquid and Ice on Phase Partitioning of Arctic Mixed-Phase Clouds with NCAR
1184 CAM5, Journal of Geophysical Research: Atmospheres, 124, 13071-13090,
1185 10.1029/2019JD030502, 2019.

1186 Zhang, M., Xie, S., Liu, X., Lin, W., Zhang, K., Ma, H. Y., Zheng, X., and Zhang, Y.:
1187 Toward Understanding the Simulated Phase Partitioning of Arctic Single-Layer
1188 Mixed-Phase Clouds in E3SM, Earth and Space Science, 7, e2020EA001125-
1189 e002020EA001125, 10.1029/2020EA001125, 2020.

1190 Zhang, R., Wang, H., Fu, Q., Pendergrass, A. G., Wang, M., Yang, Y., Ma, P. L., and
1191 Rasch, P. J.: Local Radiative Feedbacks Over the Arctic Based on Observed Short-
1192 Term Climate Variations, Geophys Res Lett, 45, 5761-5770,
1193 10.1029/2018GL077852, 2018.

1194 Zhao, C. F., Xie, S. C., Klein, S. A., Protat, A., Shupe, M. D., McFarlane, S. A.,
1195 Comstock, J. M., Delanoe, J., Deng, M., Dunn, M., Hogan, R. J., Huang, D., Jensen,

1196 M. P., Mace, G. G., McCoy, R., O'Connor, E. J., Turner, D. D., and Wang, Z.:
1197 Toward understanding of differences in current cloud retrievals of ARM ground-
1198 based measurements, *J Geophys Res-Atmos*, 117, Artn D10206
1199 10.1029/2011jd016792, 2012.
1200 Zhao, X., Lin, Y., Peng, Y., Wang, B., Morrison, H., and Gettelman, A.: A single ice
1201 approach using varying ice particle properties in global climate model microphysics,
1202 *Journal of Advances in Modeling Earth Systems*, 9, 2138-2157,
1203 10.1002/2017MS000952, 2017.
1204

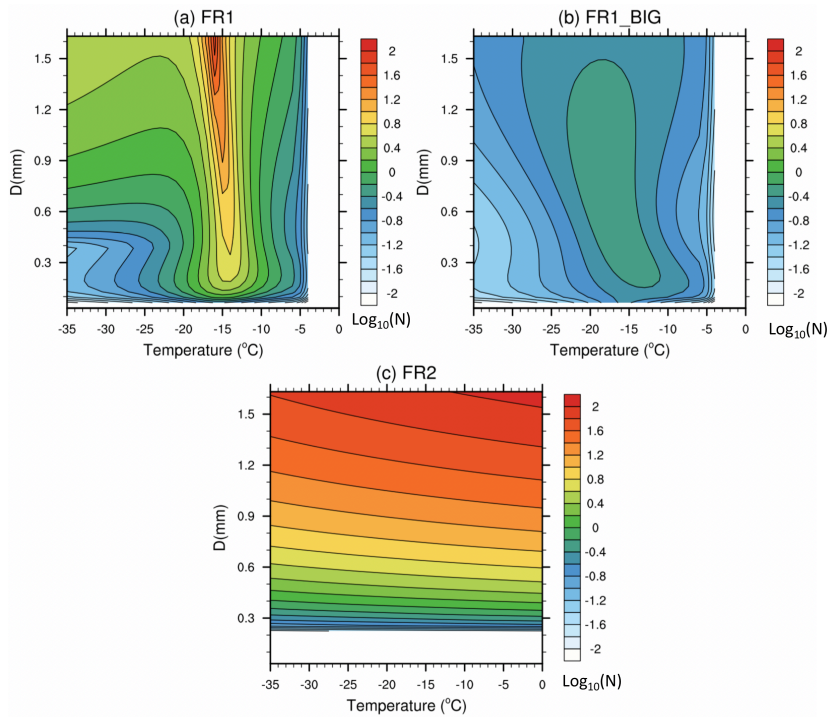


1205
 1206
 1207
 1208
 1209
 1210
 1211

Figure 1. The number of fragments per collision as a function of initial collisional kinetic energy (CKE). The ice habit is assumed to be dendrites when the temperature (T) is between -12°C and -17°C and is assumed to be spatial planar when $-40^{\circ}\text{C} < T < -17^{\circ}\text{C}$ and $-12^{\circ}\text{C} < T < -9^{\circ}\text{C}$, following Phillips et al. (2017).

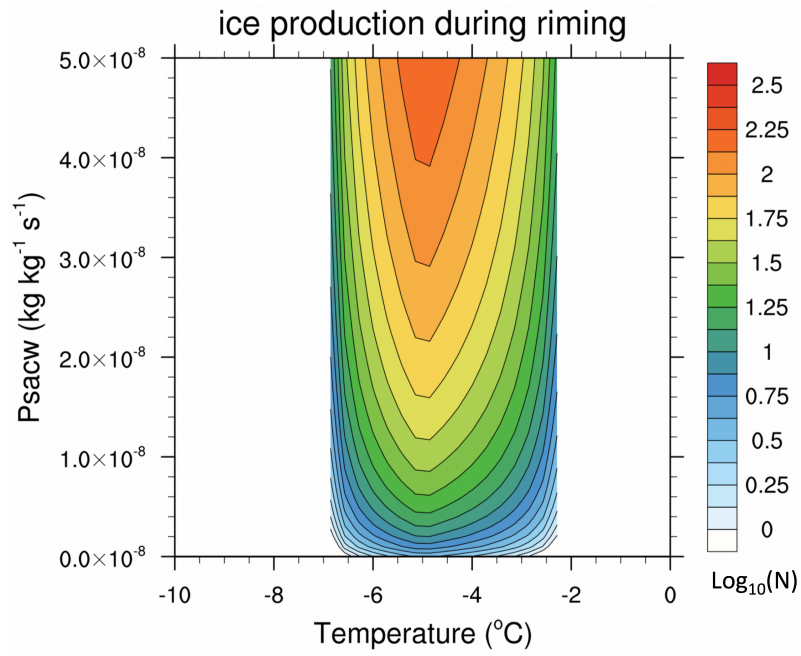
删除了: Figure 1. The number of fragments per collision as a function of initial kinetic energy (CKE).

删除了: initial



1215

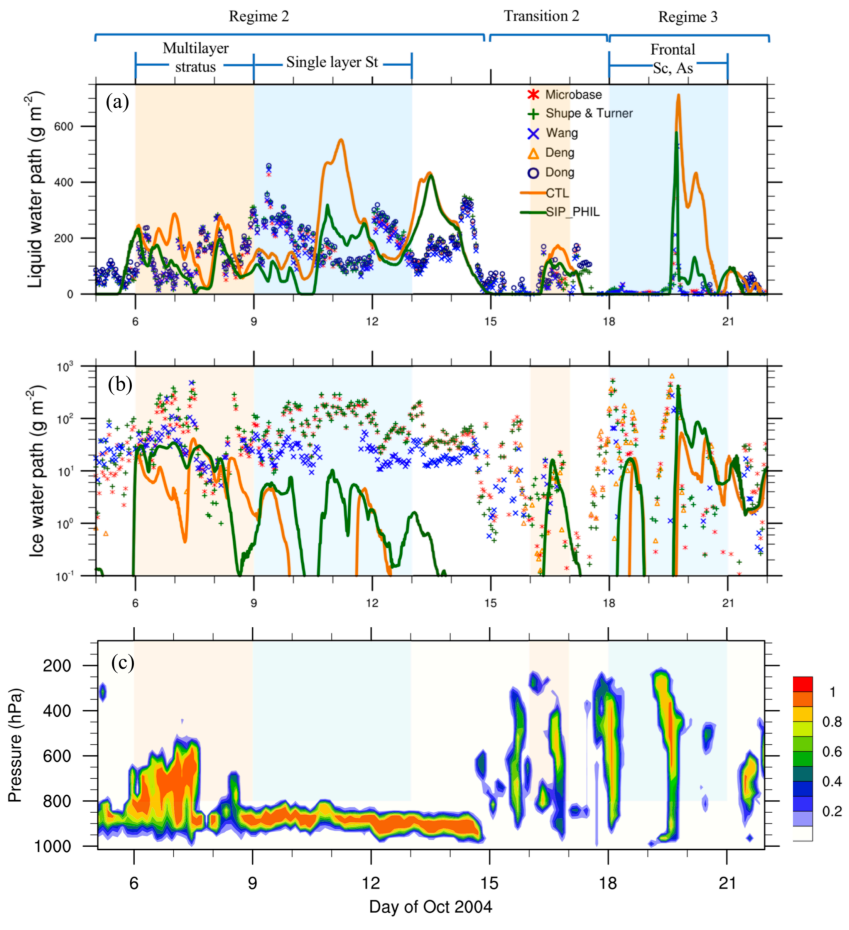
1216 Figure 2. The number of fragments per frozen drop (shown as $\log_{10}N$) as a function of
 1217 temperature and particle diameter, from (a) mode 1 of the rain freezing fragmentation
 1218 (FR1), (b) mode 1 of the rain freezing fragmentation but for the big fragments
 1219 (FR1_BIG), and (c) mode 2 of the rain freezing fragmentation (FR2).



1220

1221 Figure 3. The rime splintering rate (shown as log₁₀N) as a function of temperature and

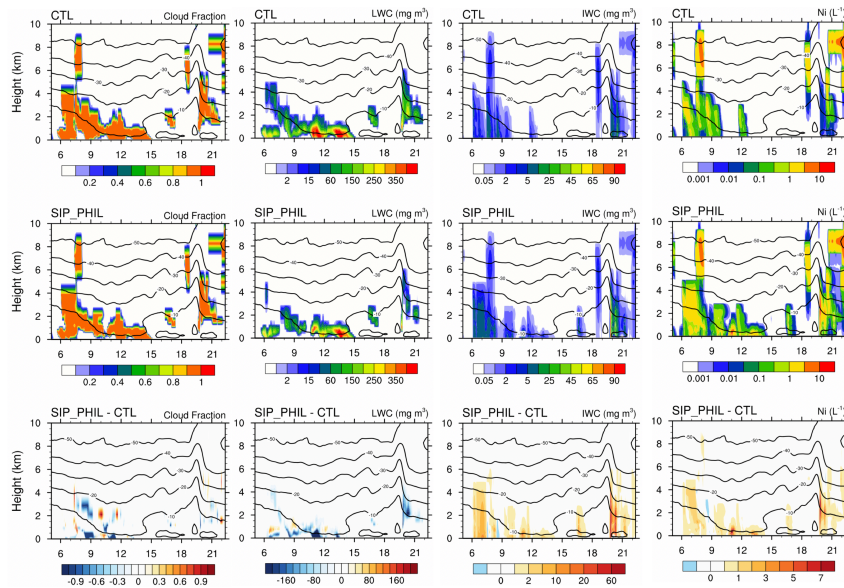
1222 riming rate.



1223

1224 Figure 4. Temporal evolution of (a) LWP, (b) IWP from remote sensing retrievals shown
 1225 as different markers, CTL experiment (orange solid line) and SIP_PHIL experiment (dark
 1226 dark green solid line), and (c) observed time-pressure cross section of the cloud fraction. The
 1227 shadings show the multilayer stratus, single-layer stratus, transition, and frontal periods.

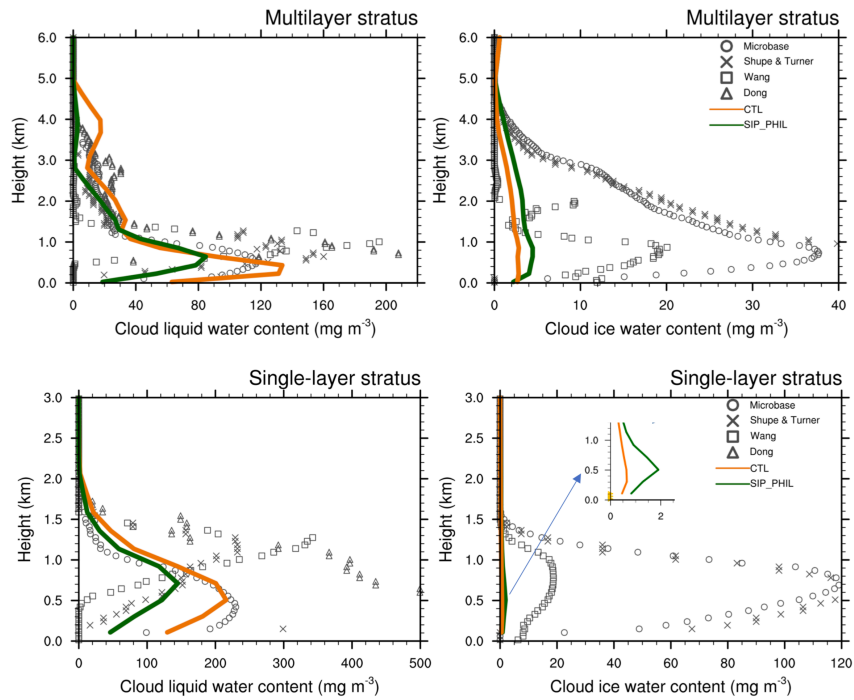
1228



1229

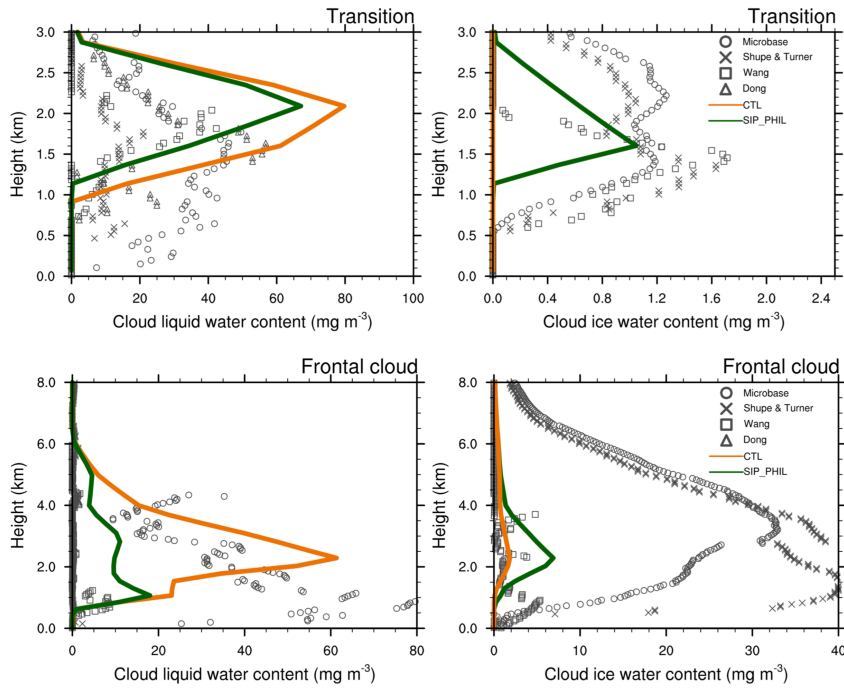
1230 Figure 5. Time-height cross section of cloud fraction (first column), LWC (second
 1231 column), IWC (third column) and ice crystal number concentration (fourth column) from
 1232 CTL (first row), SIP_PHIL (second row) and the differences between SIP_PHIL and
 1233 CTL (SIP_PHIL minus CTL, third row).

1234



1235

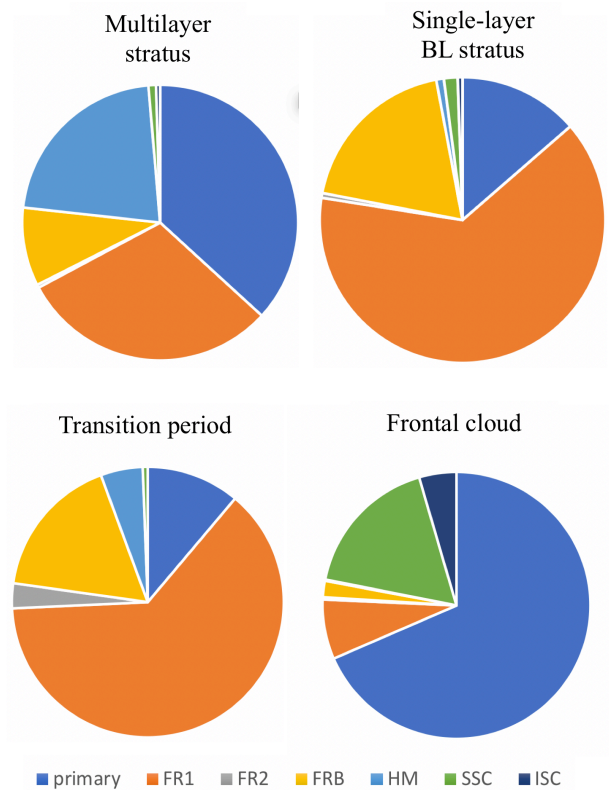
1236 Figure 6. Vertical profiles of IWC and LWC during multilayer stratus and single-layer
 1237 stratus periods from remote sensing retrievals shown as different markers, CTL
 1238 experiment (orange solid line) and SIP_PHIL experiment (dark green solid line).



1239

1240

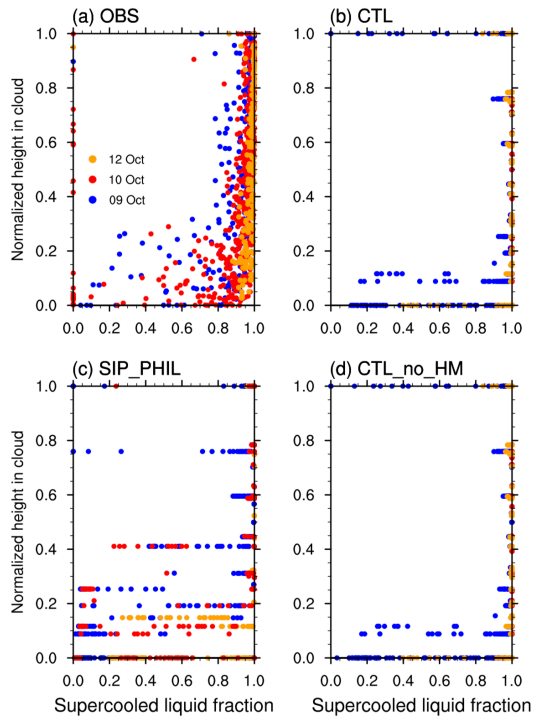
1241 Figure 7. Vertical profiles of IWC and LWC during the transition and frontal cloud
 1242 periods, from remote sensing retrievals shown as different markers, CTL experiment
 1243 (orange solid line) and SIP_PHIL experiment (dark green solid line).



1244

1245 Figure 8. Pie charts showing the relative contributions to total ice production from
 1246 primary production (i.e., ice nucleation), rime splintering (HM), fragmentation of frozen
 1247 rain (including the small fragments in the first mode (FR1), big fragments in the first
 1248 mode (FRB), and the second mode (FR2)), breakup from ice-ice collisions (including
 1249 snow and cloud ice collision (ISC) and snow and snow collision (SSC)) during the four
 1250 M-PACE periods, the vertically integrated process rates are used in the plot.

1251

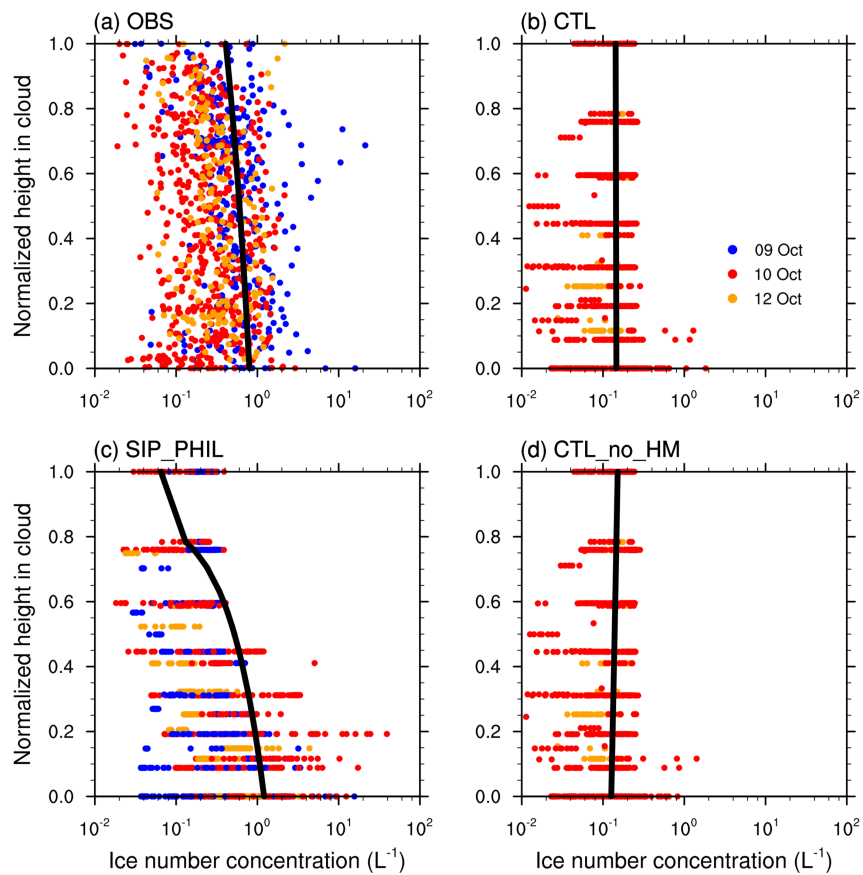


1252

1253 Figure 9. Liquid fraction as a function of normalized cloud height from cloud base. The
 1254 normalized cloud altitude Z_n is defined as: $Z_n = \frac{z - Z_b}{Z_t - Z_b}$, in which z is the altitude, Z_b is
 1255 the altitude of cloud base, and Z_t is the altitude of cloud top, from (a) observation, (b)
 1256 CTL, (c) SIP_PHIL, and (d) CTL_no_HM.

1257

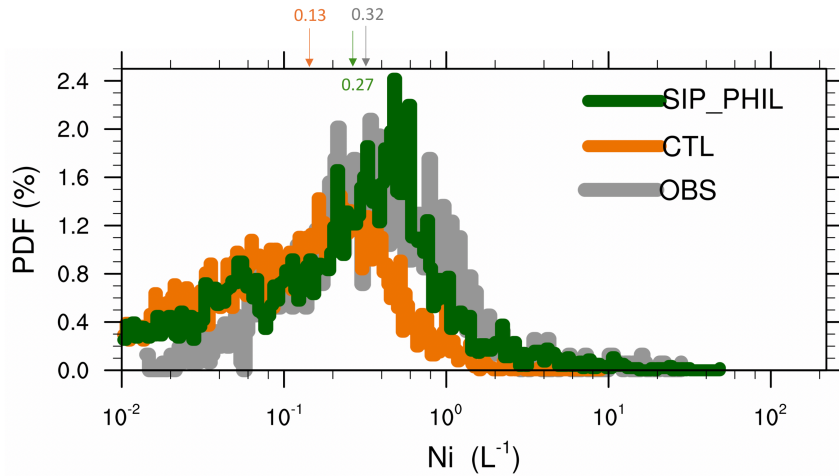
删除了: , and (c) SIP_PHIL.



1259

1260 Figure 10. Ice number concentrations as a function of normalized cloud height from
 1261 cloud base from (a) observation, (b) CTL, (c) SIP_PHIL, and (d) CTL_no_HM. Black
 1262 solid lines show the linear regression between ice number concentration and height. Only
 1263 ice particles with diameters larger than 100 μm from observations and model simulations
 1264 are included in the comparison. A correction factor of $\frac{1}{4}$ is applied to the observed ice
 1265 number concentrations shown in (a) based on Jackson and McFarquhar (2014) and
 1266 Jackson et al. (2014).

1267



1268

1269 Figure 11. The probability density function (PDF) of ice crystal number concentrations
 1270 from observation (gray line), CTL (orange line), and SIP_PHIL simulations (green line).

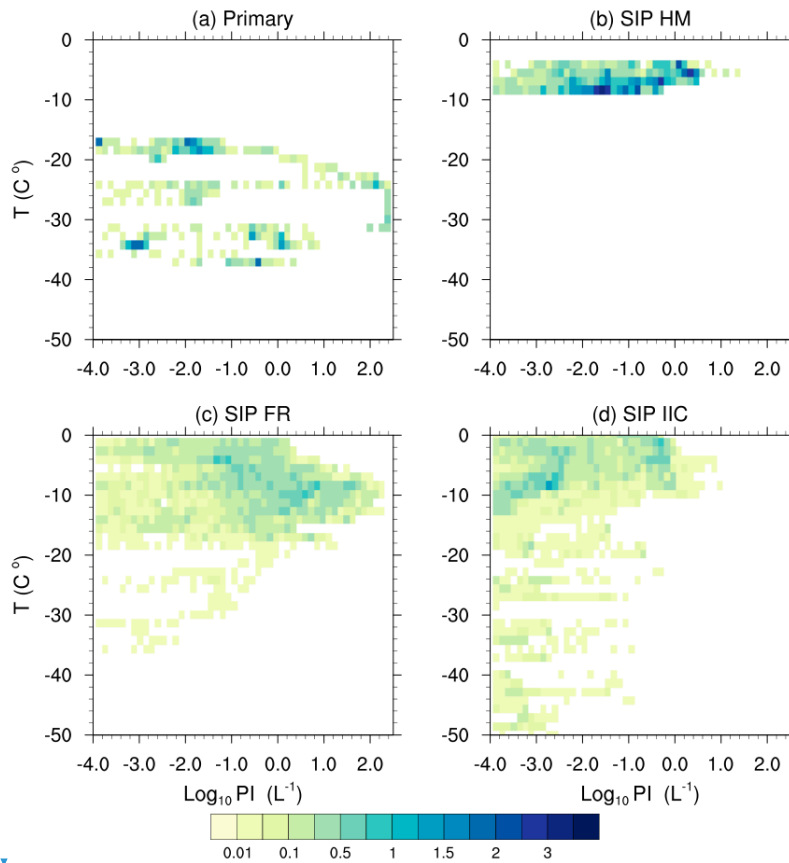
1271 The arrow indicates the median of each distribution which means that the set of values
 1272 less (or greater) than the median has a probability of 50%. [Only ice particles with](#)
 1273 [diameters larger than 100 μm from observations and model simulations are included in](#)
 1274 [the comparison. A correction factor of ¼ is applied to the observed ice number](#)
 1275 [concentrations based on Jackson and McFarquhar \(2014\) and Jackson et al. \(2014\).](#)

1276

1277

1278

1279



1280

1281 Figure 12. Bivariate joint probability density function of ice production defined in terms
 1282 of temperature and ice production, (a) primary ice production; (b) ice production from
 1283 riming splintering; (c) ice production from rain fragmentation; (d) ice production from
 1284 ice-ice collision. The ice production (PI, with unit of $\# L^{-1}$) is calculated as ice production
 1285 rate ($L^{-1}s^{-1}$) multiplied by model time step (20 mins), shown in Log_{10} .

1286

1287

删除了: Figure 12. Bivariate joint probability density function of ice enhancement defined in terms of both temperature and ice enhancement. The ice enhancement is defined as $Log_{10}(N_{SIP_PHIL} / N_{CTL})$.

删除了::

1293 Table 1. List of experiments.

1294

	Type of Secondary ice production	References
CTL	Rime splintering	[Cotton et al., 1986]
	Rime splintering	[Cotton et al., 1986]
SIP_PHIL	Ice-ice collision fragmentation	[Phillips et al., 2017]
	Rain freezing fragmentation	[Phillips et al., 2018]
CTL_no_HM	Same as CTL, but no HM process	

1295

1296

1297

1298

删除了: ↵

删除了: ing

删除了: ing

1302

1303 Table 2. The temporally-averaged IWP, LWP (unit: g m⁻²), and vertically-integrated ice
1304 crystal number concentration (unit: m⁻²) during the four periods from observation, and CTL,
1305 [CTL_no_HM](#), and SIP_PHIL experiments.

1306

		Multilayer stratus	Single-layer stratus	Transition	Frontal cloud
IWP	OBS	55.6	74.7	5.6	97.0
	CTL	11.2	0.9	0.0001	10.4
	CTL_no_HM	11.1	0.9	0.0001	8.2
	SIP_PHIL	17.1	2.5	3.6	26.1
LWP	OBS	134.4	190.2	58.3	50.2
	CTL	165.1	217.6	88.4	127.6
	CTL_no_HM	166.0	218.0	88.4	129.8
	SIP_PHIL	102.8	131.0	62.1	41.2
ICNC	CTL	5.77 × 10 ⁶	3.22 × 10 ⁵	7.66	2.26 × 10 ⁶
	CTL_no_HM	5.70 × 10 ⁶	3.17 × 10 ⁵	0.77	1.57 × 10 ⁶
	SIP_PHIL	7.09 × 10 ⁶	1.30 × 10 ⁶	4.57 × 10 ⁵	4.67 × 10 ⁶

1307

1308

1309

1310

1311 Table 3. Percentage of occurrence of liquid, mixed-phase, and ice clouds during single
1312 layer mixed-phase clouds from observation, and CTL, [CTL_no_HM](#), and SIP_PHIL
1313 experiments.

1314

	Liquid	Mixed-phase	Ice
OBS (%)	16.0	62.7	22.3
CTL (%)	73.0	26.9	0.1
CTL_no_HM (%)	73.0	26.9	0.1
SIP_PHIL (%)	40.8	58.0	1.2

1315

1316

删除了:

